

# A Double-field Computation Model to Simulate Physical Systems

Philip B. Alipour\*, T. Aaron Gulliver

Department of Electrical and Computer Engineering, University of Victoria, P.O. Box 1700 STN CSC Victoria BC, V8W 2Y2, Canada

## ARTICLE INFO

**Keywords:**

Double-field computation  
Transition probability  
Field lens distance  
Field lens coding  
Lens coding algorithm  
Entropy

## ABSTRACT

A double-field computation (DFC) model is proposed to simulate systems on any scale. A single field to DF transformation model [1–7] is proposed to simulate sampled particles from an external system to an internal system as a heat engine. The DFC measures a lens distance between two thermal events. This distance-based lens coding between events, provides an observer the information needed to detect and predict system phase transitions (PTs). This model simulates the doubling of state transition (ST) probabilities by combining a quantum circuit with a spin Hamiltonian model as the internal system. The lens coding technique results in reducing the uncertainty of the particle energy states by *doubling* their probability outcome via particle entanglement between both systems. For example, slow particles are sampled from the external system where their speed is reduced to a Bose-Einstein condensate (BEC), as opposed to classical STs occurring within the high-energy range. The DFC simulates a CNT-lens contact building quantum bit (qubit) registers as ionic traps (of BEC particles) to record particle states. The recorded data shows which portions of the system are occupied by the same particles that are not participating in a PT. Recording this information by qubit registers is valuable when it concerns heat engines. For instance, energy paths for a PT can be created or rerouted by focusing or defocusing the probability distribution of states via lenses in the DFC model to reach an isothermal temperature in the system,  $\Delta T = 0$ . A thermal event from e.g., a combustion event can be observed with maximum efficiency as particles selectively by the DF lens code burn out and flow into the engine.

## 1. Introduction

Computational models use computer programs to simulate and observe systems using mathematics, statistics, physics and computer science [8]. For example, the application of computational thermodynamics [4–6] can simulate the thermodynamics of a classical or quantum system and its state variables denoting refrigeration and combustion events, programmed from quantum computing models like [7]. This includes the state as a function of its internal and external properties e.g., energy components, with (non-)equilibrium states and its driving forces for internal processes.

In this paper, a double-field computation (DFC) model is proposed to simulate and measure thermodynamic variables based on our current research and data on a DF model [1–3].

In a quantum DF (QDF) model, as discussed in [1, 3], a Bose-Einstein Condensate (BEC) occurs when a gas of atoms is cooled until the de Broglie wavelength of the atoms becomes comparable to the distance between them [24], as a calculable thermodynamic variable. A number of researches on BEC of atoms inside bundles of carbon nanotubes (CNTs) have been conducted to observe quantum effects [48–50]. One of which is the effect of quantum statistics, e.g., Bose-Einstein statistics [84] relative to inter-particle interactions that depend on distant particle attraction and repulsion resulting in a phase transition (PT). Another research was reported as no exciton BEC effect in individual CNTs [71]. One can benefit from a quantum system made up of CNTs, lenses and magnetic field components (forces of external and internal fields as in the Ising model [57, 58]) affecting particles to produce a quantum effect, as well as measuring the statistical distance between them. Predictions of particle

states can be made by recording state transitions (STs) contributing to a PT in the system. One notable research by Friss *et al.* [53] demonstrates the entanglement of 20 qubits that work as a quantum computer using qubit registers [16, 26, 40]. A state readout of a qubit register can be compared to the simulated graphs on the quantum mechanical Hamiltonian models, e.g., the Ising model [16, 57–61]. This model can scale up to any dimension for each part of the system where a physical dataset on particle states is being sampled. A recent research as an identical replacement of CNTs can be made as boron nitride nanotubes (BNTs) for quantum sensing and storing qubits at room temperature [22, 23]. This is an ideal alternative material for our proposed system model below, using CNTs as BNTs in constructing a more efficient engine.

To simulate entanglement creation, as in [51–53, 65, 66], or predict it, a DFC *observer* has to observe a pair or more particles fall into a specific energy state of the system. An observable macrostate of  $N$  particles can be observed from the classical PT (CPT) against some or all of them falling into a ground state matter (GSM, such as BEC), as a quantum PT (QPT), [16, 58]. A set of quantum microstates from a QPT, contributes to the macrostate, or,  $\text{QPT} \leftrightarrow \text{CPT}$  [3].

In this paper, a two-part quantum field lens coding system is simulated, as proposed in Fig. 1. The first part is the CNTs as quantum light sources and detectors by applying He and Zhang *et al.* models to, respectively, generate photonic probes (in short, *photoprobes*) and detect them from the system environment [1–3, 46, 56]. A photoprobe field as particles associated with light-emitting and receiving fields can carry the momentum of a BEC, a non-BEC, or entangled BEC EPR (Einstein-Podolsky-Rosen) pairs as quantum information exchanged in the system [3, 64, 66]. The second part is based on the probability distribution of states between the CNT layer and the quantum field lensing

\*phibal12@uvic.ca (P.B. Alipour)

ORCID(s): 0000-0003-1037-018X (P.B. Alipour)

layer with sensors. This part includes the production of BEC and entangled states relative to electric and magnetic field nano-sensing from models by e.g., [47–53, 55]. As a result, a thermodynamic system is proposed and simulated to measure system efficiency on any scale by using photoprobes, field lenses, and an adder Hamiltonian (controlled Pauli-X, CNOT, or CCNOT gates) [26, 40, 51–54]. From these model elements, a QDF lens coding algorithm (QF-LCA) can be implemented equivalent to a QDF circuit, as presented in our coding method [2, 3]. Furthermore, the equilibrium and non-equilibrium states of the system can be determined by observing events through the quantum field lens relevant to the heat engine findings on thermal systems [25, 107].

The DFC simulates system components: concave and convex lenses, a pair of (super)conductors and an array of CNTs, altogether determine STs, record and cause them in an experiment. The lenses *focus* and *defocus* the distribution of particle states based on particle momentum (wavevector)  $\mathbf{k}$ , which describes a photon carrying the average particle momentum relative to its position  $\mathbf{r}$  [19]. The expected position-momentum correlation is denoted by  $\langle \mathbf{kr} \rangle$ , which contributes to the system's final energy state [1, 41]. This state, via LCA functions, is encoded in a sequence of particle states based on their entanglement probability contained within their DF [3]. This field extends between the (super)conductor pairs [48], the lenses, and particle sites as a QDF. The prediction of the next system state is made if the code sequence is decoded by a photoprobe readout of the field. This is the data obtained on any scale from qubit registers [1–3, 40, 53] via an interaction length-based scalar  $\kappa$  between those sites. The scalar defines a field transformation for  $N$ -particle spins that have flipped and contribute to the change in energy for a PT. Particle entanglement can be determined when the correlation between  $\mathbf{r}$  and  $\mathbf{k}$  is measured by photoprobes in superposition via photodetectors.

A QF lens “focusing effect” can be produced within a QPT, e.g., from laser cooling with nano-particles producing BEC at room temperature [47, 55, 73]. This is achieved by a convex lens coding of particle states. A “defocusing effect,” however, is produced via a concave lens coding. A continuous observation is simulated on the sum of combinations of these effects, which results in a QDF lens coding model. The QDF model can be used to efficiently predict a system state by measuring entanglement entropy (EE) [19, 77].

From [3], a QDF circuit is implemented to denote a  $\kappa$ -based QDF transformation relative to the algorithm's expected output, such as entanglement, which is encoded into layers (lens functions), and run on an  $N$ -qubit machine. The first layer initializes a quantum Fourier transform (QFT). In the second layer, the  $\kappa$ -based QDF transforms a field based on the momentum operator  $\hat{\mathbf{k}}$  to a third layer. This layer can be the inverse quantum Fourier transform ( $\text{QFT}^{-1}$ ) for decoding qubits [26, 97], which is a quantum state readout by a photoprobe. By observing the scalar operation, the QF-LCA can be trained through a classification scheme (a machine learning form) as a quantum artificial intelligence (QAI) technique [90, 97–99, 109]. In this technique, a classifier

provides a decision point value [102] which denotes the quantum lens distance  $d \sim |\mathbf{r}|$ -based classifier built in an intelligent decision-support system (IDSS). This is achieved by recording qubit data which are weighed, labelled and assigned to the classifier to determine the system output with a high ST probability. An observer can then predict and decide for a desired system (spin) Hamiltonian to create or reroute energy paths by the heat engine components, as discussed in [106–110] and [3].

This paper is organized as follows: Sec. 2 presents the aim and objectives of this research. Section 3 discusses the system model. Section 4 introduces the measurement of the system's thermodynamic elements to determine STs and PTs. Section 5 discusses the thermodynamic metrics performed across the system. Section 7 discusses the entanglement scaling behaviour of the system's heat engine. Section 6 is the coding algorithm with principle examples used in our model as quantum codes and the steps needed to carry out measurements. This is followed by DF lens products and analysis in Sec. 8. A method article [3] with this research discusses a quantum lens code written in a quantum assembly language (QASM [26, 99]) as a non-deterministic and deterministic algorithm. The QF-LCA in the article proposes a quantum classification scheme for tracking and training data points to predict a system state by implementing the QDF transform and EE measurement. Section 9 summarizes our conclusions. The visualized summary of the DFC model for QF-LCA is presented in Appx. A, while Appx. B presents this work's popular summary.

## 2. Aim and objectives

Photoprobes are simulated to measure particles' average momentum  $\langle \mathbf{k} \rangle \rightarrow 0$  as small (a long wavelength or red shift) and read a large value  $\langle \mathbf{k} \rangle \rightarrow \infty$  (a short wavelength or blue shift) as they exchange energies between the opposing thermal sides of the system, Figs. 1 and 3. A photon in its probe field is detected by a photodetector, and its readout can provide information about a desired Hamiltonian from an expected measurement, e.g., which particle state is needed to be measured from a focused distribution of that state?

- **Aim:** Measure any thermodynamic system parameter based on entanglement coding and entropy.
  - ⊗ The requirement is to simulate the scale of the observation of a given energy input  $E_{\text{in}}|\Psi\rangle$  to the energy output  $E_{\text{out}}|\Psi\rangle$  within the system, where  $\Psi$  is the wavefunction for a position-based particle, like a fermion inside a lattice Ising model [58], [16, Chaps. 3, 7].
  - ⊗ If one or more particles are not participating in a system's refrigeration or combustion event (a thermal event or PT), one needs to question whether the system is acting inefficiently based on the expected event?
- **1st objective:** Determine the energy path of the unfocused distribution of states through particle entanglement measure. Then, reroute the energy path by focusing its distribution through lenses. This satisfies

a desired Hamiltonian from particles contributing to an efficient system performance.

- **2nd objective:** Satisfy the 1st objective by recording and separating (labelling) particle energy states into groups of ground states (GS) and excited states (ES). The recording is when the CNOT operator acts on the input state in a qubit register as an adder Hamiltonian.

The register simulated by DFC consists of at least one trapped *slave particle* with a *slave Ising spin* [38, 39, 54]. This involves the pairing of the fermion operators to a boson field  $\Phi$ , as  $\mathbf{k}$ -based. An atom's spin flip by a CNOT operator operating on the QDF is counted by the slave boson. Definition 1 below, defines the QDF transform from [1].

**Definition 1.** A scalar DF is a field where its spatial dimensions are doubled by a pairwise field scalar operation. This operation collapses the field to its pair with an ST probability of  $P(\Psi \leftrightarrow \Phi) = |\langle \Psi \Phi \rangle|^2 \ni \langle \mathbf{kr} \rangle$ , where  $\langle \Psi \Phi \rangle$  is the QDF correlation function. The field dimensions cancel out, if via  $\kappa, \mathbf{k}$  and  $\mathbf{r}$  correlate as  $|\mathbf{kr}| \rightarrow 1$ . This is satisfied by a photoprobe state projection onto a pairwise particle state [1]. The QDF transform is implemented in [2, 3].

A DF into QDF is correlated by its correlation function  $\langle \Psi \Phi \rangle \rightarrow 1$ , if field component  $\mathbf{k}$  or  $\mathbf{r}$  multiplied by  $\kappa$  have  $|\mathbf{kr}|$  converging to a constant  $|\mathbf{k}|^2 = 1$ . This is due to a planewave travelling along  $\mathbf{k}$ , which reciprocally satisfies a QDF transformation and its measurement outcome. This scalar operation satisfies any field mapping  $\Psi \leftrightarrow \Phi$ , as discussed in Sec. 4.1. To gain a desired Hamiltonian (output) [40, 53], the particle state is separated and transitioned into the focused distribution of states for the next registered ST (spin flip) cycle, as presented by Eq. (22) in Algorithm 2.

### 3. System model simulation

In Fig. 1, the simulated thermodynamic system is split into two systems  $A$  and  $B$ . System  $A$  has particles in a mixed state made up of ground state (GS)  $|0\rangle = \begin{bmatrix} 1 \\ 0 \end{bmatrix}$  and excited state (ES)  $|1\rangle = \begin{bmatrix} 0 \\ 1 \end{bmatrix}$ . System  $B$ , as the thermodynamic inside area, is the heat engine in contact with  $A$  as the outside area or an external system for sampling particles from  $A$ . The slit is closed at this point. System  $B$  is in a GS, and contains a BEC particle using the techniques presented in [48, 65, 66].

The magnetic slit opens in this simulation. From system  $A$ , particles are sampled in system  $B$ , given their energy states. This is where a PT switch is turned on for a thermal event. A laser beam is used to project photons onto the sampled particle state. The projection forms particles as a GSM, BEC, or BEC EPR pairs in a magnetic field trap [65, 66]. The aim of this trap is to maintain the frequent production of photons (between an exciton energy level and GS level) using single-walled CNTs (SWCNT) while in contact with glass and a metal conductor, e.g., gold nanoparticles in a lattice [46–48].

The slit is once again closed. Quantum states are generated based on the probability distribution of states between the CNT layer and the quantum field lensing layer. Particle superposition becomes entanglement (via a CNOT gate) [18], and can be determined between particles in  $A$  and  $B$  by photoprobes as their photon fields are generated in  $B$  from the SWCNT layer, Fig. 1(f) via 1(c). A pair of SWCNTs are contacted to a superconductor [48] to satisfy the entanglement of qubit pairs from superposition, which occurs at the coupled concave-convex lensing point. The contact builds a CNOT gate [40, 44], where the control qubit is the polarization of a photoprobe field, and the target qubit is the photoprobe (energy) path with degrees of freedom [52]. The convex and concave lenses, respectively, focus and defocus the distribution of particle states for determining and predicting the next particle state, as particles exchange energy with each other (the *lens work*, as discussed in Sec. 6). Additionally, by applying a CNOT gate between a sampled atom and the photon from its photoprobe field, entangles these two particles [40, 52], which operates on quantum superposition and not just on classical basis states.

In this simulation, the slit remains closed as the two-level dye molecule is pumped by an intense field of photons generated from the CNT layer and convex lenses. Surface excitations from the lattice propagating along a metal nanoparticle array on glass produces BEC, with the possibility to observe entanglement via a superconductor connected to a pair of CNTs, Figs. 1(d)–1(f). The distribution of low-energy states on one side of the CNT pair against high-energy states on the other side, is shown in Fig. 1(e). The voltage drops between the CNT pair causing entanglement between particles [45, 48]. The qubit state of slow particles in  $A$ , paired with the qubit state of the sampled particles in  $B$ , is encoded into an ES within a QPT or a crossover to a CPT, if the expected system's final state is determined as ES via BEC EPR pairs, Fig. 1(g) or Fig. 3(b). Conversely, the qubit state is encoded into a GS for all BEC atoms [1].

The slit opens after a lensing event on the sampled particles flowing out from  $B$  to  $A$  for further interaction, energy release and gain (excitation or absorption). Systems  $A$  and  $B$  via the superconductor and photodetector [56], expect to receive a re-emitted photon from an atom after projecting the photon from  $B$  onto the atom's path or space in  $A$ . Entanglement is detected between the state of a sampled atom in  $B$  (CNOT gate), paired with a particle state in the demarcated areas between Figs. 1(a), (d) and (g). This applies to  $n$  sampled particles in system  $B \leq N - n$  particles in system  $A$ . If all  $N$  particles are sampled, then entanglement occurs within system  $B$ . The inequality returns  $2n \leq N$ , which links  $n$  sampled particles to  $2n$ -EPR pairs between systems  $A$  and  $B$ , as entangled qubit pairs.

The DFC simulates entanglement in a qubit pair stored between  $A$  and  $B$  based on  $2^N$  parallel operations (computational basis states [16, 40]) on  $N$  qubits via CNOT gates in  $B$ . Superposition becomes entanglement as  $\mathbf{k}$  and  $\mathbf{r}$  correlate between qubit pairs satisfying a Bell state [1, 3, 18, 20]. This gives  $\log_2 2^N = N$  qubits =  $2^w - w$ , where each

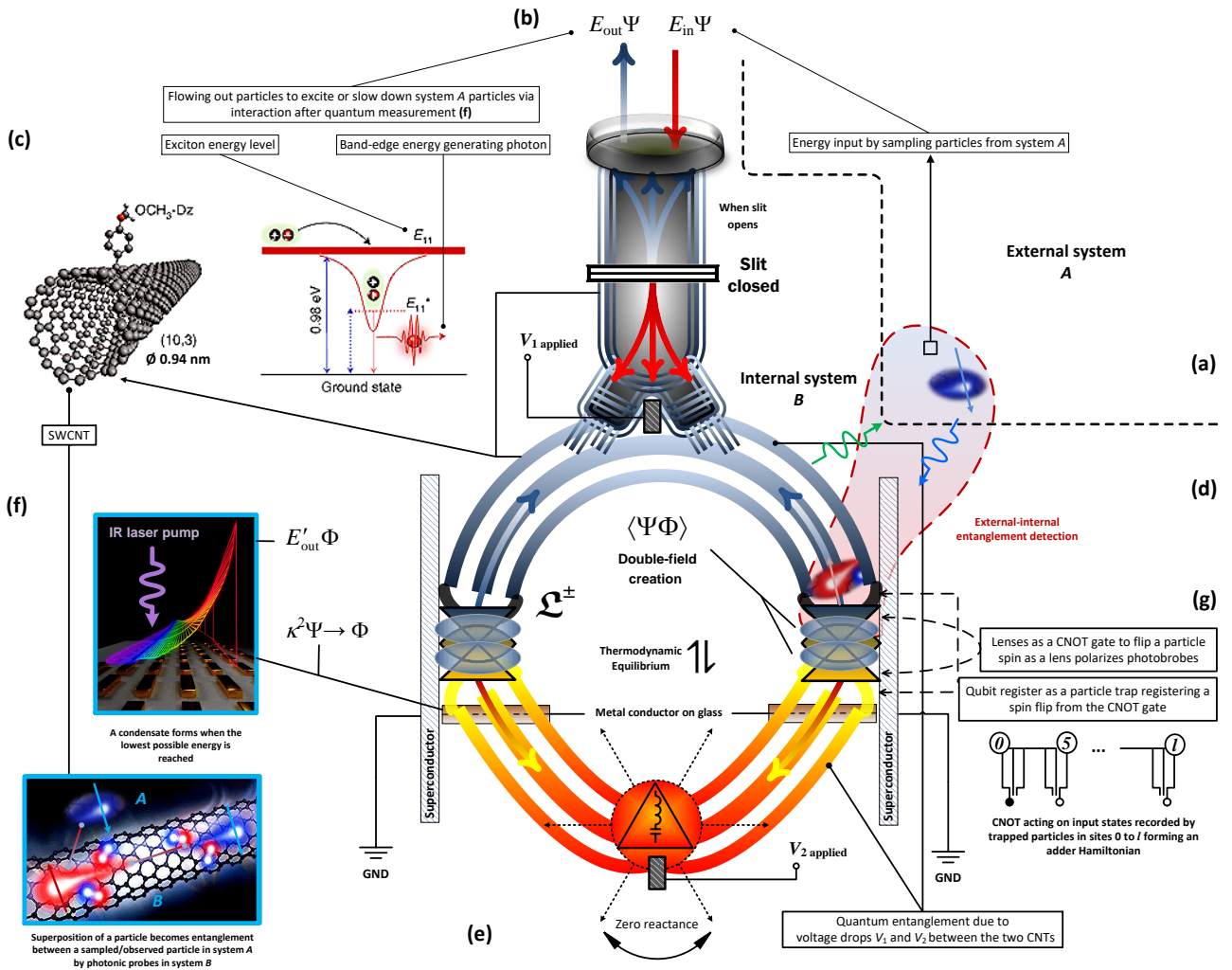


**Fig. 1:** DFC simulates system measurement and efficiency by the proposed lenses and photopropes: **(a, b)** Measurements are done within the internal system **B** after sampling particles from external system **A** where the slit is closed. The slit opens after a lensing event on the sampled particles from system **B** to system **A**. **(c)** Photons are generated in a  $(10,3)$  SWCNT as photoprobes (photons in a probe's field) to conduct measurements. **(a, d)** External-internal entanglement of a paired particle is detected by a photodetector installed on the superconductor observing the QDF transformation between **A** and **B**. **(e)** There is a zero reactance to voltage drops between the two superconducting points in **B**, as temperature reaches a critical point for a PT. The resultant heat is absorbed by resistors in the CNT layer. As the frequency increases, the reactance of the capacitor decreases, and at a BEC point increases for a proper readout of energy states of BEC atoms. **(f)** A set of superposing particles entangle within the system, where photoprobes are detected by photodetectors for a readout. Each measurement readout is from an entangled pair, where their entanglement is scaled between two or more DF points, Eq. (8). **(g)** Lenses function as a CNOT gate to (dis)entangle particles relative to **(d)-(f)** events contributing to a QPT. An adder Hamiltonian is formed by trapping particles that record which CNOT operator acted on the input state. The black dot is one of the CNOT operators that has acted on a possible 3-qubit input (CCNOT), while the rest remain in a BEC or state  $|0\rangle$ . The count is to measure how many times entanglement has occurred. The input denoting entanglement is the black dot, and the rest of the gates are the inverse (no entanglement/white dots). The photoprobes are later used to decompress the count by reading the state of the trapped particles e.g., EPR pairs into classical states. A quantum decoherence of classical states is obtained by a gradual diffusion of BEC at a QPT level, Example 4.

qubit state has the complex number  $w$  subtracted from  $2^w$  complex numbers, or added to the real numbers describing the system's GS and ES. The branch point for the principal branch is at  $w = -1/e$ , with a branch cut that extends to  $-\infty$ , as  $N \rightarrow \infty$ . Hence, the system performs  $2^N$  parallel operations in **B** correlating with **A** [40] by particles in the adder Hamiltonian, Figs. 1(d)–(g). The real solution is based

on the Lambert's  $W$ -function [32] for any complex number

$$w = [-W_{\pm m}(\pm \log 2/2^N) - N/\log 2] / \log 2 \geq -N, \quad (1)$$

where  $\pm m$  is a plus or minus quantum integer denoting the amount of quantum data gathered [34] by a photoprobe in **B** as qubits from **A**. For  $-m < 0$ , the values of  $w \in (0, N)$ -particles denote the information is projected from **A** to **B**. The principal branch [32] of function  $W_{\pm m}$  is formed by the

$\pm$  momenta (information) projected between  $A$  and  $B$ . This is the projection of states from  $A$  as information gathered by particles in  $B$  for qubit data processing.

**Remark 1.** The choice of the logarithmic base in Eq. (1), depends on evaluating the system state by measuring the average entropy of the amount of incoming bits, qubits, or energy STs [103–105] in the system per unit of time or cycle. This is conditional to the user of the QF-LCA loading classical data into a quantum state, and vice versa [105].

From the spin models in [57, 60, 65], BECs are generated in a periodic array of potential wells and CNT bundles [61–63]. A uniform curvature of these CNTs (helical shape) exhibits ferromagnetic properties at high temperatures [72], useful to determine when the neighboring BEC particles in a lattice site are about to change their spins at a QPT level, Fig. 3. As a result, BEC is obtained on the low temperature side, Figs. 1(f) and 1(g), and a quantum communication channel is established to transmit quantum information between  $A$  and  $B$  via a  $\kappa$ -based QDF transformation.

In Fig. 2, the creation of a DF is labelled and simulated in the center of the heat engine based on field lenses and their projection of states (lens products) from Fig. 1(g). The quantum information transfer for each projection is denoted by a qubit teleportation between an input state and an output state, and its inverse is to achieve this information via superdense coding. The implementation of QDF is the core component of the QDF circuit and compatible with QFT transformations [3]. The examination of a QDF transformation depends on observing the correlation value between momentum and position in the QDF measurement component  $\langle \mathbf{kr} \rangle$ . This component is for pairwise particles with a probability to interact with more particles. This probability measure associated with  $\langle \mathbf{kr} \rangle$ , provides a classification system between distinguishable and indistinguishable states from the simulated QDF circuit [3, Tables 3–5].

Predictions on STs with probabilities  $\geq \frac{2}{3}$  are made over the simulated quantum channel between entangled EPR pairs based on scalar  $\kappa$  transforming their QDF to a classical field. This contributes to *teleportation* [18, 66] establishing communication between particles prior to a QPT, Fig. 1(f). A predicted state is classified based on calculating EE [19, 46, 58], after particle sampling [3, Eqs. (34)–(37)].

## 4. Thermodynamic element simulation

An event is defined as an ST, like a particle *spin transition* (flip) on a magnitude of  $|j|$  event occurrences (event frequency) that contributes to a PT, where  $j$  is the particle's  $j$ -th state. To determine a CPT or QPT, the system's *thermodynamic elements* need to be *measured* using photoprobes and photodetectors to record system events as a lens coding technique [3]. This measurement can be simulated by applying the following operations relative to each element.

### 4.1. Element measurement

1. Measure particle (average) momentum relative to position, or, equivalently, frequency [19].

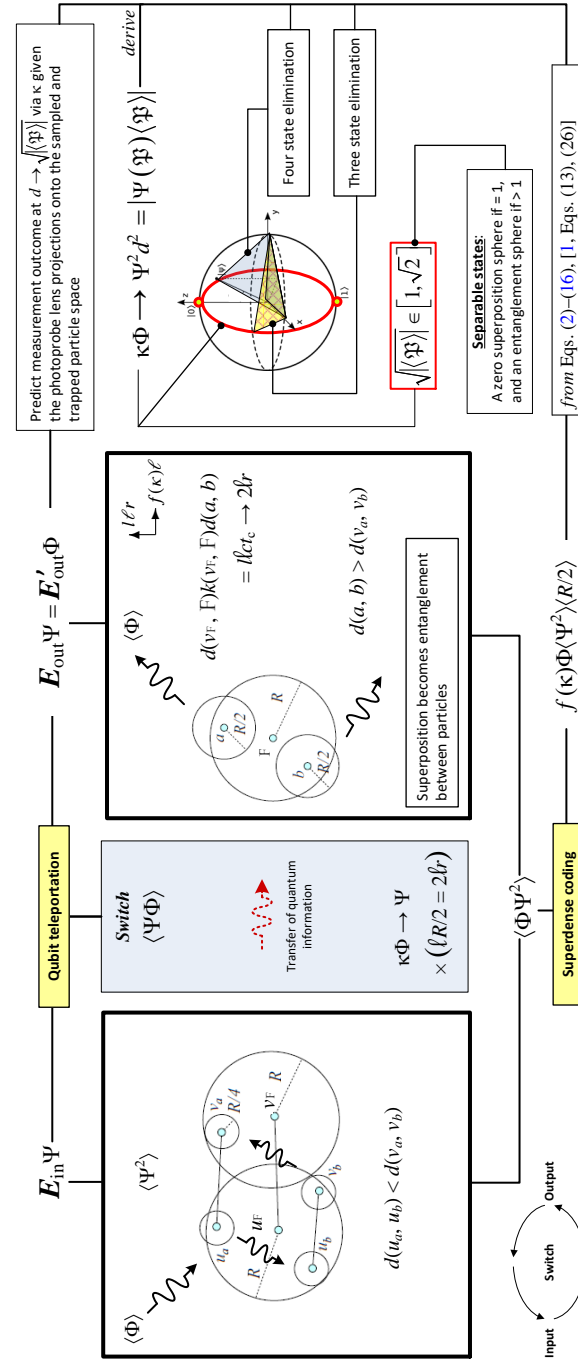


Fig. 2. A theoretical framework according to the QDF model proposed by [1], corresponding to the lower figure and Fig. 4 events. The model focuses on particle pairing, entanglement and the predictions of states under a QDF transformation.

2. Measure the expected correlation  $\langle \mathbf{kr} \rangle$  in  $\langle \Psi \Phi \rangle$  as particles pair up from their sites within or between systems  $A$  and  $B$  as a QDF. Site  $l$  has a particle in state  $i$ . A neighboring site  $l'$  with a probability to have a particle, can pair up and entangle with the particle in site  $l$ , as described by quantum state  $|i_{ll'}\rangle$ .
3. Measure the statistical distance in qubits by defining EE, [46, 58, 80], between the quantum lens products generated from particle sites in systems  $A$  and  $B$ .
4. Apply CNOT to the sites for recording particle states toward the final state of the system.

5. Measure EE, where a CPT or a QPT is determined from the encoded entangled states between a sampled particle in  $B$ , paired with a particle in  $A$ , i.e., from the entanglement detection area in Figs. 1(a) and (d).

*1st and 2nd measurements*— A moving particle has an average position of  $\langle \mathbf{r} \rangle$ , and when interacting with another particle in superposition, has a probability to entangle with that particle if paired within their quantum field [16, 31]. A paired particle field firstly, has the quantum field of average positions  $\langle \Psi \rangle$ , given that  $\Psi$  has the dimensions of  $L^{-\frac{3}{2}}$ , where  $L$  is the length of a pairwise site for a particle pair to interact with each other. Secondly, the field has particle momentum measured from the average momenta  $\langle \Phi \rangle$ , where  $\Phi$  is the wavefunction for a  $\mathbf{k}$ -based particle like a boson (a photoprobe) projecting onto and off of lattice fermions. The dimensions of  $\Phi$  are defined as  $L^{\frac{3}{2}}$ , where the particles of this field scale a pairwise site by its inverse length  $L^{-1}$ . Hence, the correlation between  $\mathbf{r}$  and  $\mathbf{k}$  forms a QDF correlation function  $\langle \Psi \Phi \rangle$ . The correlation scales between the output, the PT switch as the magnetic slit in Fig. 1, and the input in Eq. (11) can be determined by measuring the ST probability of the field transformation. The magnetic slit opens and particles from system  $A$  are sampled based on their energy states in system  $B$ . This is where a PT switch is turned on for a thermal event. This measurement is from a distance between two field points,  $a$  and  $b$ ,

$$\begin{aligned} \lim_{|\mathbf{kr}| \rightarrow 1} d(a, b) \ell |\mathbf{kr}| &= d(v_F, \mathbb{F}) k(v_F, \mathbb{F}) d(a, b) \rightarrow d(a, b) \ell \\ &= \ell R/2 = 2\ell r \leq l \ell c_t, \end{aligned} \quad (2)$$

where a PT decays over time  $t_c$  with some probability, Eq. (3), as  $c t_c \rightarrow \lambda_c$  after a  $\kappa$  operation, and  $d(v_F, \mathbb{F}) k(v_F, \mathbb{F}) = |\mathbf{kr}|$ . This measure is required to determine the state and position of a sampled particle relative to any other quantum particle interaction during a QDF operation. Given the least uncertainty bound discussed in [1, Sec. 4], and  $\min l = 4$  from Example 2, the quantum information exchange with some probability  $\mathcal{P}$  between two field points,  $a$  and  $b$ , is

$$\min l r \mathcal{P}_{ab} / 2 \mathcal{P}_{ba} \xrightarrow[\text{switch}]{\kappa\text{-field}} 4 \mathbf{r}_{i,j} |\langle f(\kappa) \ell \rangle| = \langle R/2 \rangle, \quad (3)$$

where  $r = |\mathbf{r}|$ , and  $\{\mathcal{P}_{ab}/\mathcal{P}_{ba}\} \rightarrow |\langle f(\kappa) \ell \rangle|$  describes a PT into a QPT or CPT as it decays over time  $t_c$ . The correlation function  $\langle \Psi \Phi \rangle$  reaches a constant as a number denoting entanglement when used by a photoprobe at the CNT layer. Any other correlation value denotes a set of particles in a disordered state (a CPT with great entropy). The QDF transform via  $\kappa$  has a direct relationship to the EE scaling of the Ising model. The length in the QDF is renormalized per QDF transformation step, and can be treated as the *number of pairwise sites*, showing how many spin pairs have been flipped (Sec. 7). The animated steps in Fig. 3 define the events of spin flips relevant to a CPT  $\leftrightarrow$  QPT by scaling  $L$  as the correlation length  $\lambda_c$  to entanglement length  $L_E$  (discussed in Secs. 5 and 7).

*3rd measurement*— The energy path creation, or the decision to reroute particle states from a disordered state of system  $A$ , in system  $B$ , is done by determining the superposition and entanglement between a set of fast and slow particles that have a net spin-up GS, as in the ferromagnetic case in Fig. 3. The paired particles are counted by

$$\mu_{ij} = (N^2 - N)/2, \quad (4)$$

which is the number of pairwise particle interactions exchanging energy states between sites  $i$  and  $i'$ . This energy exchange contributes to a QDF lensing event caused by a quantum lens which creates the  $i$ th and  $j$ th events between the two sites. The interaction length between particles via  $\kappa$ , scales to  $\mu_{ij}$  counted within  $L$ , as  $L \rightarrow [L \mu_{ij}]$ . The number of particles entangled over  $L$  scaling to  $L_E$ , is counted by the adder Hamiltonian relative to lens distance  $d$ ,

$$\mu_d = \lim_{L \rightarrow [0,1] L_E} [L \mu_{ij} / Nd]. \quad (5)$$

For the minimally entangled particles,  $L$  tends to  $L_E \approx 0$ . The particle states entangled between sites  $i$  and  $i'$  have wavevectors  $\mathbf{k}_{i_{ll'}}$  and  $\mathbf{k}_{j_{ll'}}$ , and positions  $\mathbf{r}_{i_{ll'}}$  and  $\mathbf{r}_{j_{ll'}}$ , where  $|(\mathbf{k}_{i,j})_{ll'}| = |\mathbf{k}_{i_{ll'}} - \mathbf{k}_{j_{ll'}}|$  and  $|(\mathbf{r}_{i,j})_{ll'}| = |\mathbf{r}_{i_{ll'}} - \mathbf{r}_{j_{ll'}}|$ . The non-entangled states have wavevectors  $\mathbf{k}_i$  and  $\mathbf{k}_j$ , and positions  $\mathbf{r}_i$  and  $\mathbf{r}_j$ , [1, Sec. 4]. The magnitude of the expected position product  $\langle \mathfrak{P} \rangle$  and wavevector product  $\langle \mathfrak{K} \rangle$ , are respectively

$$|\langle \mathfrak{P} \rangle| = |\langle \mathbf{r}_{i_{ll'}} \mathbf{r}_{j_{ll'}} \rangle| \quad \text{and} \quad |\langle \mathfrak{K} \rangle| = |\langle \mathbf{k}_{i_{ll'}} \mathbf{k}_{j_{ll'}} \rangle|, \quad (6)$$

given that entanglement is always contained in the QDF, mainly in form of these products.

The average change in momentum and change in position in each particle site relative to its pair are, respectively,

$$\langle \mathbf{k}_{i,j} \rangle = \left| \frac{1}{N} \sum_{i=0}^{N-1} \mathbf{k}_i - \frac{1}{N} \sum_{j>i}^N \mathbf{k}_j \right| = \frac{|\mathbf{k}_i(N-i) - \mathbf{k}_j(N-j+1)|}{N}$$

and

$$\langle \mathbf{r}_{i,j} \rangle = \frac{|\mathbf{r}_i(N-i) - \mathbf{r}_j(N-j+1)|}{N}. \quad (7)$$

The momentum transfer from a particle to its pair with lower energy can result in a PT as  $[\mathbf{k}_{i,j}^2]^{\frac{1}{2}} < \lambda_p^{-1}$ , [1, 74], where  $\lambda_p \approx 10^{-35} \text{ m}$  is the Planck length. This forms a  $\mu_{ij}$ -qubit code denoting  $2^{\mu_{ij}}$  states for each energy exchange made between two particles. Their QDF contains entanglement and can be decoded from the  $\mu_{ij}$ -qubit code in Sec. 6.

*4th measurement*— Entanglement is contained in the QDF. The information transmission from the QDF over a quantum channel via  $\kappa$  is satisfied by measuring the photoprobe's momentum off of a particle pair. The photoprobe-particle pair interaction increases or lowers the probe's energy state. This denotes a momentum transfer from the pair to the photoprobe, as  $|\mathbf{kr}| \rightarrow 1$ . The particles' physical information is collected by the probe on a magnitude of  $|\mathbf{r}|$ :

$$\kappa^2 \Psi = \kappa^2 \sqrt{N \rho(\mathbf{r})} e^{i \mathbf{k}_{i,j} \mathbf{r}} = \kappa^2 \psi_{i_n}(\mathbf{r}) \rightarrow \phi_{i_n}(\mathbf{k}) e^{i \mathbf{kr}} = \Phi, \quad (8)$$

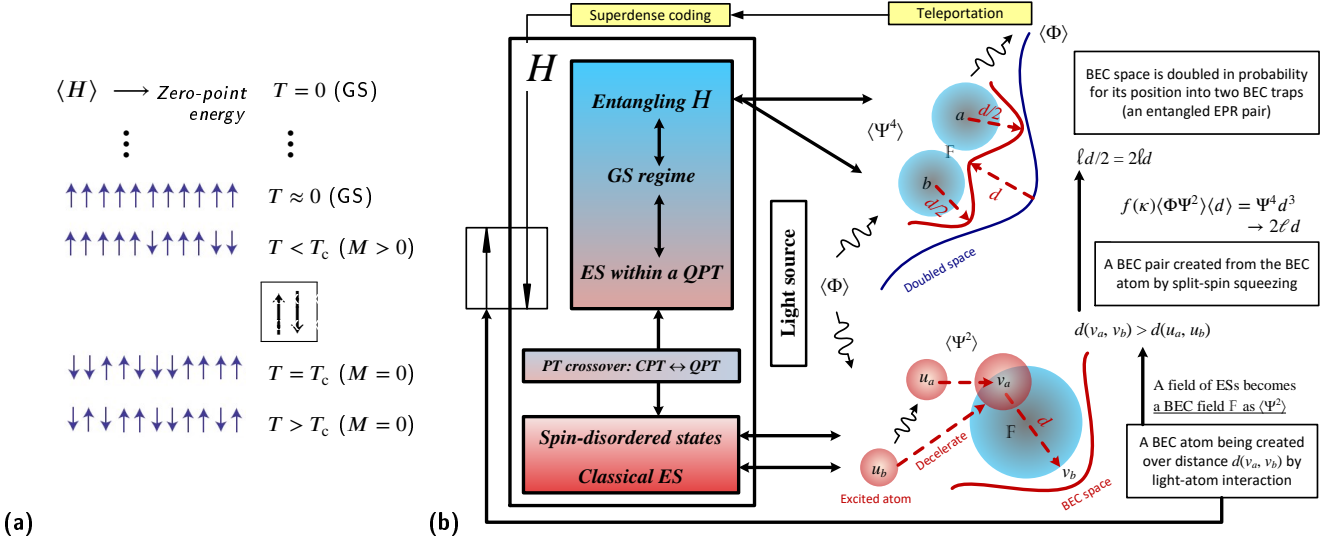


**Fig. 3:** (a) Spin ordering simulation for the Ising model, as temperature increases (top to bottom) magnetization  $M$  changes to a zero net value. The correlation length increases when temperature is decreased (ordered spins), and diverges at critical temperature  $T_c$ . If the external field is absent ( $h = 0$ ), there is still  $M = 0$ , [16, 19, 42, 43]. (b) The cyclic production of BEC via atom-light interactions with an expected spin order in (a), to create BEC EPR pairs in an entangling Hamiltonian Eq. (24), scaled from  $H$  in Eq. (23), from an ES to a GS regime. Their space in probability doubles in a correlated QDF, Eqs. (2)–(16), as opposed to a disordered non-BEC space. Teleportation is performed after doubling, and the classical states are decoded by sharing EPR states via superdense coding. Notably, shades of red and blue, respectively, denote excited and ground states, contrary to the blue and red shifts colored in Figs. 1 and 4.

where  $i$  is the imaginary unit, and state  $i_n$  corresponds to the  $n$ th particle which assumes state  $i$  in its site, and  $\varrho$  determines the probability (density) that the particle in state  $i$  will be found at position  $\mathbf{r}_i$  via  $\mathbf{k}_{i,j}$ , Eq. (7). The transformation is “reciprocal” via a  $\kappa^{-2}$ -operation, given the convergence for that  $n$ th particle by pairing it with other particles to gather information about  $\mathbf{r}$ . The ES  $|i\rangle = |1\rangle$  can be determined by its scattering factor  $e^{i\mathbf{k}_{i,j}\mathbf{r}}$  through the photoprobe’s field  $\Phi$ . The GS  $|i\rangle = |0\rangle$  can be determined by the condensate density  $\varrho(\mathbf{r}) = |\Psi|^2$ . This is achieved by observing STs, prior and after a PT, caused by a DF switch, as discussed below.

**Remark 2.** The focus of the theoretical aspects of the lens coding algorithm is on scaling the input and output qubit operations as the building blocks to simulate and implement a deterministic (predictive) quantum circuit [3].

**Remark 3.** For all quantum cases in the QF-LCA, the values of  $i$  and  $j$  are limited to  $j(j \leq i) \in [0, 2]$ , where the value 2 denotes any GS or ES of a particle’s quantum state  $\{|0\rangle, |1\rangle, \dots, |N-1\rangle\} \mapsto |2\rangle$ . This determines a QPT or a crossover to a CPT [21], Sec. 4.2 and Example 4.

*5th measurement – All particles contribute to the system’s total energy  $E$  (or the Hamiltonian  $H$ ) as*

$$E = E_{i_m} + \sum_n^N E_{i_n}, \quad i_m \leq i_n, \quad (9)$$

which is the sum of  $(N + 1)$ -particle energies, or  $E_{i_n}$  of  $N$  particles and  $E_{i_m}$  of a particle in a trap, or entangled with its

pair as in Example 2.B, or see, Figs. 1(a), (d) and (g). The levels of particle energy  $E_{i_m}$  can be written as

$$E_{i_m} = E_0(2mi_m + 1), \quad m \in [1, \infty], \quad (10)$$

where an observer of system  $B$  can assume  $m$  quantum states for the quantum particle. This measurement is satisfied only if  $m$ -level  $j$  states are characterized by the principal quantum number, as any other interacting particle during a quantum state transfer between traps. A complete energy readout is required to determine state  $i$ . For this, a particle’s quantum state  $n$  as  $|i_n\rangle$  can be read from  $\Delta E = E_{\text{out}} - E_{\text{in}}$ , which is the energy interval.

In Fig. 1, a PT occurs from the QDF as a tensor product  $|\psi\rangle \otimes |\phi\rangle$ . Depending on the field intensity  $\sim \lambda_c^{-2}$  resulting from photonic projections, field emissions cause a switch from one energy state to another

$$\underbrace{\langle \Psi | E_{\text{in}} | \Phi \rangle}_{\text{input}} \rightarrow \underbrace{|E_{i_n}\langle \Psi | \Phi \rangle|}_{\text{switch}} = \langle E_{\text{out}} \rangle, \quad (11)$$

where field  $\Phi$  associates a scalar value by its switch function  $f(\kappa)$  for an output state from  $\Delta E$ , which is independent of a  $\kappa$ -based field transformation between energy states. The field  $\Psi$  via  $f(\kappa)$ , and  $\lambda_c$  satisfying the field intensity, result from a photon-atom projection which can form a direct sum  $|\psi\rangle \oplus |\phi\rangle$  of the two fields  $\Psi$  and  $\Phi$ , relative to the expected values of  $E_{\text{in}}$  and  $E_{\text{out}}$ . In the switching process, the expected energy output is lower than the energy input,  $\langle E_{\text{out}} \rangle < E_{\text{in}}$ , where  $\langle E_{\text{out}} \rangle$  is useful [88] to an  $n$ th sampled particle if it entangles with the trapped particle. This achieves an ES as

a momentum transfer from the trapped to the sampled atom. This is expressed as

$$\underbrace{|E_{i_n}\langle\Psi|\Phi\rangle|}_{\text{switch}} \rightarrow \underbrace{|\langle f(\kappa)\Delta E\ell\rangle|}_{\text{phase transition}} = \underbrace{\langle E_{\text{out}}\rangle}_{\text{output}}. \quad (12)$$

In Fig. 1, from right-to-left, a quantum field or a PT is described by a set of wave functions

$$\mathbb{F} = \{\Psi, \Phi, \Psi^2, \Phi^2, \Psi\Phi, \Phi\Psi, \dots\}, \quad (13)$$

where a set element  $\ell \in \mathbb{F}$  is dimensionless or else, as in [35, 36]. The switching operation via  $f(\kappa)$  in Eq. (12), is

$$\Delta E = E_{i_n} - E_{i_m} = 2E_0|\Delta i|, \quad (14)$$

where  $|\Delta i| = |i_m - i_n|$  is the magnitude between the input state and output state,  $E_0$  is the zero-point energy of a quantum oscillator [41, 60], e.g., a BEC trap in Figs. 1 and 3. The system's expected energy can be calculated from  $|\Delta i|$ , given  $i_m$  and  $i_n$  values, which determine  $i$ . Thus,  $\langle E_{\text{out}}\rangle$  is predicted as the change  $\Delta E\ell$  in a QPT from Eq. (12).

## 4.2. Operations for phase and state transitions

A CNOT gate operates on a qubit pair, entangles or disentangles Bell states [1, Sec. 5.3]. This is expressed as a direct sum  $\oplus$ , or a tensor product  $\otimes$  of two inputs between states  $|\psi\rangle$  and  $|\phi\rangle$ , followed by the DF switch, Eqs. (11)–(14). A PT occurs per field switch as a tensor product  $|\psi\rangle \otimes |\phi\rangle$  satisfying a qubit pair with a product state  $|i_m\rangle \otimes |i_n\rangle = |i_m i_n\rangle$ , given  $\mathbf{r}_{i,j}$  and  $\mathbf{k}_{i,j}$  from Eq. (7). This tensor product represents the  $AB$  space, and captures all the dynamics of particles that interact in that space, as described by their density matrix [112]. The direct sum stacks up the value of each observable (a state), so the quantum states on the output side can be separated and measured as the particles diffuse from their product relative to  $\lambda_c$ . The sum returns a target qubit to an assumed state  $|i_n\rangle$  by the  $n$ th particle in system  $B$ . The control qubit in CNOT remains unchanged, and is in a GS or state  $|0_m\rangle$  for any trapped particle. The target qubit flips, only if the control qubit is  $|1_m\rangle$  set by a photoprobe for a QPT or CPT counted by a slave particle. The qubit data are used to determine  $i$ . The QPT  $\rightarrow$  CPT occurs if  $|1_m\rangle \rightarrow i = 1$  via  $j$ , as  $i_m \leq i_n$  from Eqs. (8)–(14). The tensor product is calculated after an energy readout from Eq. (9), which is an ST product  $|i_m i_n\rangle \rightarrow |i j\rangle$ .

## 5. Thermodynamic metric simulation

The correlation between  $\mathbf{k}$  and  $\mathbf{r}$  is measured by the DF as a QDF correlation function  $\langle\Psi\Phi\rangle$ , Sec. 4 and Def. 1. From this measurement, the quantum state of particles can be determined as the correlation length  $\lambda_c$  diverges at a critical point (a PT) [21], which can scale to  $\lambda_p$  [1, 74, 76], for a QPT. The simulated measurement is generated wherever the DF as a QDF is formed, such as particle pairing [38] at the lenses (a combination of concave and convex lens functions). The QDF transform has the following ST probability

$$\mathcal{P}(\Psi \leftrightarrow \Phi) = |\langle\Psi\Phi\rangle|^2 \sim |\langle\Psi(\lambda_p)|\Phi(\lambda_c^{-1})\rangle|^2 \geq 1/2. \quad (15)$$

The correlation function  $\langle\Psi\Phi\rangle$  is equal to 1, if DF component  $\mathbf{k}$  or  $\mathbf{r}$  multiplied by  $\kappa$  satisfies the conversion of  $|\mathbf{kr}|$  to a constant  $|\mathbf{k}|^2 = 1$ . This is due to a planewave travelling along  $\mathbf{k}$ , which reciprocally satisfies the expected QDF transformation [1]. From Eqs. (7)–(13), a field transformation

$$\kappa\Phi \rightarrow \kappa^{-2}\Phi\ell r = |\Psi(\mathfrak{P})\langle\mathfrak{P}\rangle|, \quad (16)$$

constructs a QDF which denotes  $\Phi$  transforms into  $\Psi$  via  $\kappa$  relative to  $\lambda_c$  and  $\lambda_p$  at sites  $l$  and  $l'$ . As  $|\mathbf{r}| \rightarrow \lambda_p$ ,  $\lambda_c = |\kappa^4\mathbf{r}^{-1}|$  diverges to  $\infty$  at a critical point (PT), [21, 74, 76]. The projection of an output state from  $\Phi$  onto the input state from  $\Psi$ , provides the photoprobe with a linear superposition having an ST probability  $\geq \frac{1}{2}$ . To determine the length divergence, the quantum lens distance  $d$  between two lensing events needs to be measured as defined below.

**Definition 2.** A DF lens function  $\mathfrak{L}$  as  $\mathfrak{L}^+$  takes all particle states from sites  $l$  and  $l'$ , and gives 1 convex (focused) product of  $m$ -level  $j$  states with an  $\mathbf{r}_{m;j_{ll'}}$  (super-)position. Function  $\mathfrak{L}$  as  $\mathfrak{L}^-$  takes all particle states and returns a concave product of states with  $\mathbf{r}_{i,j}$  positions. A mix of concave and convex products is a product of a convex-concave lens function  $\mathfrak{L}^\pm$ .

**Definition 3.**

- a) A DF lens product is the result of a *lens work*. The *work done* is the energy transfer from a lens to focus or defocus energy states for a particle, to gain or lose momentum via a pairwise interaction. The work is done when a lens product is observed over a lens distance  $d$  relative to lengths  $\lambda_p$  and  $\lambda_c$  between fields  $\Phi$  and  $\Psi$  of Eq. (15).
- b) The DF lenses *force* the photons that are generated from the external CNT layer to focus and defocus the distribution of particle states. This is achieved by projecting the photons onto a path of atoms based on correlation  $\langle\Psi\Phi\rangle$  between their average momentum  $\langle\mathbf{k}\rangle$  and average position  $\langle\mathbf{r}\rangle$ .
- c) CNTs, lenses and the magnetic field components as forces of *external* and *internal fields* (Ising model [57, 58]) affect particles to produce a GSM and provide the measurement of the statistical distance between them.
- d) A series of GSM productions from a broad range of GSs can scale to the production of a BEC from a specific GS in a trap [1, Remark 8]. An entangled BEC EPR pair [65, 66], created at a lens distance of  $d$ , each BEC of the pair is a DF lens product observed over a quantum communication channel relative to  $d$ .
- e) The distance for the quantum channel scales to entanglement length  $L_E$  between the entangled EPR pair, and is evaluated for any  $d$  between two lens products that can scale to  $L_E$  in a QDF circuit [3].

The lens distance as a function between two lens products via lensing events, STs and PTs, one as a micro-level, and the other as a macro-level observation within the system is

$$d(\mathfrak{L}^-, \mathfrak{L}^+) = \left| \mathfrak{L}^-(N)\mathbf{r}_{i,j}^2\lambda_c^{-1} - \mathfrak{L}^+(N)\mathbf{r}_{m;j_{ll'}}^2\lambda_p^{-1} \right|, \quad (17)$$

where the unit  $\iota = \iota^{4n+1}$  is used to describe the photoprobe field projecting onto the particle pair space relative to  $\lambda_p$  [1], as the possible *quantum measurement point* [1, Sec. 2.2]. This is expressed by  $|\mathbf{r}_m| \gtrsim \lambda_p$ , which denotes a photon from its probe field travelling at light speed  $c$  across a magnitude of Planck positions in the lattice, where a counter particle (trap) is formed as a GSM or BEC. The photoprobe carries the frequency of a sampled particle from as measured by  $\langle II' \rangle$ . The notation  $\mathbf{r}_{j_{II'}}$  is used to denote particle entanglement in Eq. (7). In the QDF (Ising) model,  $\mathbf{r}_{j_{II'}}$  alters to length  $L$ , scaling to entanglement length  $L_E$ . This length scales as  $\lambda_c$ , which diverges at a critical point as  $|\mathbf{r}| \rightarrow 0$  and  $\lambda_c \rightarrow \infty$ , according to Eq. (15). A  $\mathbf{k}$  to  $\mathbf{r}$ -based field transformation from Eq. (15) has an ST probability

$$\mathcal{P}(\Phi \rightarrow \Psi) \approx 4(N-1)^2 / 9\vartheta_{ij}\mu_{ij} \geq 2/3, \quad (18)$$

where  $\vartheta_{ij} \in [\frac{8}{9}, 1]$  is the pairwise particle adjustment factor adjusting the result against the irreducible  $\frac{8}{9}$  produced for a big  $N$  [1]. This probability is determined for  $N$  interacting particles sampled from an input state of a  $\mathbf{k}$ -based field  $\Phi$  describing a photon, coupled with an output state of an  $\mathbf{r}$ -based field  $\Psi$  describing an atom, Eq. (17). The adjustment factor  $\vartheta_{ij}$  is applied due to one particle of the pair *misbehaves* (uncontrolled) within the given interval  $[\frac{8}{9}, 1]$ . The trapped particle behaving within the range of the interval is superposing with  $\approx 0.1$  or  $10\%$  level of uncertainty, which is  $\geq 90\%$  probability to be in position. Thus, an ST probability of  $\mathcal{P}(\Phi \rightarrow \Psi) \approx 1$ , is by projecting and coupling an input state with an output state, Fermi's golden rule [69], based on superposition between the free and trapped particles [1].

The converse of Eq. (18),  $\mathcal{P}(\Psi \rightarrow \Phi)$  with the same range of probabilities is determined based on the sampled atoms for the input state, paired with an output state of a photoprobe for an atomic state readout.

From Eq. (4), there are  $\mu_{ij}$  pairwise interactions in a QDF for either field transformation  $\Psi(\mathbf{r}) \rightarrow \Phi(\mathbf{k})$  or  $\Phi(\mathbf{k}) \rightarrow \Psi(\mathbf{r})$  in Eq. (8). These interactions for Example 2.B events, results in 6 positions: 2 photonic superpositions projected from light at the beam splitter (lens) onto an atom's space with two positions where photoprobe Eve observes, and 2 atomic positions from the atom after it splits as a BEC EPR pair. The ratio of occupying positions in carrying the quantum information by the EPR pair via the beam splitter interaction [3, 65], is 8 : 9. In total, with the entangled EPR state, there are  $6 + 2 = 8$  parts of quantum information shared with an extra entangled qubit as an exciton. This returns a ratio of 8 : 9 parts of information exchanged between particles at the superconducting contacts with a pair of SWCNTs, Fig. 1. Figure 1(f) shows where a laser infrared (IR) pump contributes to a BEC production [16, 47] and the multiple positions relative to entanglement between systems  $A$  and  $B$ , Fig. 1(d), or pairwise positions of entangled pairs in a QPT as shown in Fig. 3(b).

The value of  $f(\kappa)$  in Eq. (12) is determined relative to the 6 particle positions quantified in Eq. (18), with a ratio of  $\alpha^2 = \{4\mathbf{k}_{i,j} : 2\mathbf{r}_{i,j}\}$ . Their probability density function is

$\rho = \rho(\mathbf{k}_{i,j})$  or  $\rho(\mathbf{r}_{i,j})$ , which ranges between the upper and lower bounds of the scalar  $|\kappa^2|\rho \leq 2$ , [1]. The bounds of scalar  $\kappa$  rewrites the ST probability from Eq. (15) as

$$\begin{aligned} \mathcal{P}(\Phi \leftrightarrow \Psi) &= f(\kappa)|\langle \Psi | \Phi \rangle|^{\pm 2}/2 \\ &= f(\kappa)\rho/2 \in [|\kappa^2\alpha|^{-2}, |\kappa^2\alpha|^2]/2 = (0, 1], \end{aligned} \quad (19)$$

which can be used in a density matrix to determine  $N$ -particle entanglement generated from superposition. An ST probability  $\geq 2/3$  denotes a QPT at  $\lambda_p$ , and denotes a CPT at a distance of  $d \gg \lambda_p$ , [1].

## 6. DF lens coding algorithm

The code, based on a DF lens operation, is comprised of qubits that represent the information about the transition between an input state and an output state, as well as their lens distance to determine an ST probability  $\geq \frac{2}{3}$ , Eq. (18).

### 6.1. Algorithm code definitions and examples

**Definition 4.** In a binomial trial [69], and from Def. 2, a lens output state  $o$  is observed after an ST with probability 1, which is a successful classical state (or a failed quantum state) outcome. The opposite outcome of any trial is a mixed output state. Its density matrix representation has a probability  $p < 1$  for  $|0\rangle$  or  $|1\rangle$ .

**Definition 5.** The entropy of the reduced density matrix  $\rho_A$  (equivalently  $\rho_B$ ) is EE as  $S(\Psi_{AB}) = S(\rho_A) = -\text{tr}(\rho_A \log \rho_A)$ , which counts the number of entangled bits between systems  $A$  and  $B$ , where  $\rho_A = \text{tr}_B \rho_{AB}$ , and  $\text{tr}_B$  is the partial trace of a pure or a mixed system state  $\rho_{AB}$ . For a pure state,  $\rho_{AB} = |\Psi\rangle\langle\Psi|_{AB}$ , and  $S(\Psi_{AB}) = S(\rho_A) = S(\rho_B)$ , where  $|\Psi\rangle_{AB} = |\Psi\rangle_A \otimes |\Psi\rangle_B$  is a joint state [58, 68].

**Example 1.** If systems  $A$  and  $B$  each have  $n$  qubits, then in a maximally entangled state,  $S(\rho_A) = n \log 2$ .  $S(\rho_A)$  counts the number of bits, or  $e^{S(\rho_A)}$  counts the number of entangled states (since  $n$  qubits have  $2^n$  states) [16, 80]. The entanglement contained in  $|\Psi_{AB}\rangle$  between  $A$  and  $B$  is measured by  $S(\Psi_{AB})$ . This as the quantum information can be used to simulate the creation or rerouting of energy paths for a set of particles not participating in a thermal event.

**Example 2.A.** A light source emits random polarized photons through a lens as a polarizing beam splitter, which changes the path of a photon if its polarization is in a polarization state flipping an atom's spin. This is a control qubit forming a CNOT gate, and the target qubit is the path of the same photon hitting the atom [52]. The density matrix for the state of photons is  $\rho = |\phi\rangle\langle\phi|$ . For each step of polarizing the photons horizontally (control qubit) with an up path (target qubit) state  $|0\rangle$ , or vertically with a down path state  $|1\rangle$ ,  $\rho$ 's index is incremented by 1. The density matrix for the emission is  $\rho_1 = \frac{1}{2}|0\rangle\langle 0| + \frac{1}{2}|1\rangle\langle 1| = \begin{bmatrix} 0.5 & 0 \\ 0 & 0.5 \end{bmatrix}$ . From Def. 4, the lens output  $o = \text{tr}(\rho_1^2) = 0.5$  is observed as a mixed state. If a second lens function as a CNOT gate is applied, a vertical

plane polarizer disentangles the photons. The lens output is  $o = \text{tr}(\rho_1^2 \rightarrow \rho_2) = 1$  which is scaled up to the maximum value of scalar  $\kappa$  for the pair,  $|\alpha\kappa^2|^2 \rightarrow 2$ , Eqs. (8)–(17). This achieves a pure state expressed by a density matrix  $\rho_2 = d|\kappa^2\alpha|^2 = 2\mathcal{L}^+\rho_1 = L_{\mathcal{E}}\begin{bmatrix} 1 & 0 \\ 0 & 0 \end{bmatrix}\begin{bmatrix} 0.5 & 0 \\ 0 & 0.5 \end{bmatrix} \approx 2\begin{bmatrix} 0.5 & 0 \\ 0 & 0 \end{bmatrix}$ . This result is obtained due to the maximum distance scaled to  $L_{\mathcal{E}}$  between the paired photons. The polarization is done twice as two lensing events, with an event frequency (see Sec. 8.2) of  $|j|^2 = (2\text{nd and 3rd ST}) = 2$ , to fully polarize the mixed state. The final event is a pure vertical state at the maximum length scale of entanglement, which is detected by the photodetector. The atom's state is recorded with probability 1, denoting zero entropy.

From Refs. [65, 66] and Defs. 3c) and 3d), Example 2.A can be simulated and expanded to the following example:

**Example 2.B.** From Example 2.A, photonic entanglement can be prepared by a beam splitter operation [65]. In Figs. 1(f, g), this beam splitter is simulated as DF lenses and its interaction with particles between the lenses and the metal conductor where lasing and BEC are produced. Among the simulated sampled particles in system  $B$ , BEC is produced in a trap, Figs. 1 and 3(d). The beam splitter operation is applied on single mode squeezed states generating a two-mode squeezed state as two spatially separated BECs from a BEC in two traps (boxes) [65, 66]. This corresponds to an entangling Hamiltonian between  $l$  and  $l'$  in the system with a spin-spin Bell state correlation, see Eq. (24). This is the entanglement between BECs produced by splitting a single squeezed BEC into two spatially separated BECs. Alice via the box, as an EPR pair, can represent the sum of Bell correlations up to  $(4/\sqrt{2}) = 2\sqrt{2}$  from the four possible combinations of Bell states  $|ij\rangle_{ll'} = \{|00, 01, 10, 11\rangle\}_{ll'}$ . The pair can perform a quantum teleportation, e.g., Alice as the sender of the qubit information on the prize state to a box as the receiver. The box with the prize, can teleport its state to another box. Alice and the box resource, which is the prize state, is shared as the EPR state with Bell correlations observed within a BEC, and between the EPR pair [66]. Alice mixes her input state with her EPR state at the beam splitter which can function as a CNOT gate, Example 2.A. Alice then sends the qubits through the CNOT gate, and the first qubit through a Hadamard gate. Alice performs a Bell measurement on her qubits obtaining one of the four Bell state results, and sends the classical result (two classical bits) to the box. The box from this classical result performs a phase-space displacement on its GS mode (half of the EPR pair) to recover the original unknown input state and change or unchange the prize state. The prize state remains entangled with Alice, or becomes (transitioned into) a GSM or a BEC in one of the boxes. This teleportation can be performed between the pair through the QDF compatible components: QFT and  $\text{QFT}^{-1}$  which implement the interaction potential and kinetic energy operators on states  $|i_{ll'}\rangle$  and  $|j_{ll'}\rangle$ , see EE encoding from [3]. The same QDF components are used to perform the inverse of teleportation as *superdense coding*

[3, 79] to decode the EPR state in the QDF circuit, Figs. 1–2. Other parties e.g., Eve can share the EPR state from the entangled pair with Bob to see which box is with the prize.

**Remark 4.** In Example 2, the maximum value of  $\kappa$  via  $\alpha$ , denotes the ST probability applied to a pairwise field over length  $L$ , doubles the probability in the density matrix through a lens function, achieving a pure state.

From Example 2 and Eq. (19) [1, Sec. 6], the following intervals for Eq. (16) can be derived

$$\Psi(\mathfrak{P}) \geq 2^{-\frac{1}{2}}, \text{ and } |\langle \mathfrak{P} \rangle|^{\frac{1}{2}} \in [1, \sqrt{2}], \quad (20)$$

where separable states or zero superposition can be observed once  $\mathbf{r}_{j_{ll'}}$  is predicted via  $\kappa$  as  $|\langle \mathfrak{P} \rangle|^{\frac{1}{2}} \rightarrow 1$ , as well as entanglement, if  $|\langle \mathfrak{P} \rangle|^{\frac{1}{2}} > 1$ , [27]. From Sec. 5, for each diverging length  $L$  between a pair of particles (strictly measured between a pair of positions in sites  $l$  and  $l'$ ),  $\mathbf{r}_{j_{ll'}}$  can scale to  $|\langle \mathfrak{P} \rangle| \xrightarrow{L} L_{\mathcal{E}} \approx 2$ .

## 6.2. Coding steps and example

The DFC algorithm simulates entanglement observed from an  $N$ -body quantum state  $|\psi\rangle$  between systems  $A$  and  $B$ , Figs. 1(a) and 1(d). From one EE measurement to another in a PT loop, the  $N$ -body state is encoded into a product state of a Schrödinger's cat state (in short, a cat state) [3, 16, 26, 44, 51]. The encoding is implemented by superdense coding between particle pairs. In Algorithm 2, steps 1(a)–(b), the control qubit in the CNOT operation is a photoprobe that can flip the state of an atom to disentangle or entangle the atom (due to  $h > 0$ ) with another atom via particle interaction. This CNOT operation includes producing BEC (a GSM) from a classical state, using the same photoprobes that target an atom's spin to flip [3, 47, 55, 73].

**Example 3.** System  $B$ 's inside area, Fig. 4(a), is a particle site. This area is partitioned into four observable quadrants (as in the unit circle) of energy surface  $\mathcal{O}$ , spanning from the energy input phase  $E_{\text{in}}\Psi(t)$  to the energy output phase  $E_{\text{out}}\Psi(\tau)$ . In the classical case, the input states are given in four observable quadrants of energy surface  $\mathcal{O}_{q \leq 4} = \{\mathcal{O}_1, \mathcal{O}_2, \mathcal{O}_3, \mathcal{O}_4\}$  in systems  $A$  and  $B$ . The inside area sites of parallel quadrants of energy surface  $\mathcal{O}_{q \leq 4}^{\parallel} = \{\mathcal{O}_1^{\parallel}, \mathcal{O}_2^{\parallel}, \mathcal{O}_3^{\parallel}, \mathcal{O}_4^{\parallel}\}$  as quantum, Fig. 4(a) left, in  $B$ , can map to inside area sites 2 and 3 of  $\mathcal{O}$  via the photoprobe field  $\Phi$ , Fig. 4(a) right, corresponding to the Fig. 4(b) flow diagram. This is defined as  $|\Psi(t)\rangle_{\mathcal{O}^{\parallel}} \xrightarrow{\Phi} |\Psi(\tau)\rangle_{\mathcal{O}} |1\boxed{11}1\rangle$  with the inside area sites 2 and 3 outlined (boxed) in the center, and outside area as sites 1 and 4. The density matrix is  $\rho = |1\boxed{11}1\rangle\langle 1\boxed{11}1|$ . Hence,  $\rho_B = \langle 0|_1\langle 0|_4\rho|0\rangle_1|0\rangle_4 + \langle 1|_1\langle 1|_4\rho|1\rangle_1|1\rangle_4 = |11\rangle_{23}\langle 11|_{23}$ , and  $S(\rho_B) = -\text{tr}(|11\rangle\langle 11| \log |11\rangle\langle 11|) = -\text{tr} 1 \log(1) = 0$ . This corresponds to Fig. 4(b) as an internal ST  $\rightarrow$  CPT occurrence in system  $B$  with probability 1 as a non-entangled state. In the quantum case, the area covers  $E_{\text{in}}\Psi$  in all parallel quadrants of  $\mathcal{O}_q^{\parallel}$

---

**Algorithm 1:** DFC of entanglement entropy and system efficiency

**Require:** Use the  $N$ -body quantum state based on the Hamiltonian  $H$  from Eq. (23).

**Ensure:** Construct the corresponding reduced density matrix  $\rho = |\psi\rangle\langle\psi|$  as the output.

- 1: Define the inside area of system  $B$ . The outside environment of  $B$  is system  $A$  area where particles are sampled and traced out of the density matrix:  $\rho_B = \text{tr}_A \rho$ .
- 2: Use the reduced density matrix to compute EE:

$$S(\rho_B) = -\text{tr}(\rho_B \log \rho_B) = -\text{tr}(\rho_A \log \rho_A) = S(\rho_A). \quad (21)$$

- 3: The initial state is maximally entangled if  $S(\rho_B) = \log 2$ , and not entangled if  $S(\rho_B) = 0$ , [77, 79].

- 4: Maximize system efficiency in determining the scalar behaviour of entanglement (discussed in Sec. 7) by a  $\kappa$ -based QDF transformation and doubling the ST probability in the density matrix (see Remark 4).
- 

**Algorithm 2:** DF lens coding of the  $N$ -body quantum state as a product state of a cat state and a classical state

**Require:** Input a qubit pair.

**Ensure:** Implement CNOT or CCNOT gates [3, 40] and record their input and output. Decode qubits as classical bits by the recipient.

- 1: Implement a CNOT gate and encode classical data into qubits (consistent with IBM Qiskit convention [3])
    - (a) CNOT logic: *input the qubit pair  $\rightarrow$  if the first (most significant or leftmost) qubit (control qubit) is |1>, then the cnot gate flips the second (least significant or rightmost) qubit (target qubit)*.
    - (b) Encode a bit-pair denoting  $A$  and  $B$  system state using one qubit, compress and classically record (register) the compression of any qubit sequence based on CNOT logic:  $|00 \rightarrow 00\rangle \in |0\rangle$ ,  $|01 \rightarrow 01\rangle \in |1\rangle$ ,  $|11 \rightarrow 10\rangle \in |2\rangle$ , and  $|10 \rightarrow 11\rangle \in |2 \rightarrow 1\rangle$ . The last qubit compression  $|2 \rightarrow 1\rangle$  in decimal is obtained through an IF-statement involving subtraction between the registered classical bits as  $b(11 - 10) = 3 - 2 = 1$ , see [3] code examples.
    - (c) Assign the result as a new label number (data point), see [3].
  - 2: Keep a record (a qubit by a bit-pair as in *teleportation* [16, 18, 66], i.e., the opposite of superdense coding) on which CNOT gate denoted by  $\mathbf{C}_{0 \leq s}$  operators operated on the input [40], where  $s$  is a step counted from a stepwise interval  $\Delta t^*$ . This is implemented by forming an adder Hamiltonian between the CNT layer and the lenses.
    - (a) Start counting by the adder with register qubits in the input state  $E_{\text{in}}|\Psi\rangle$ , and a counter particle (trapped)  $\mathbf{c}_{0 \leq l \leq \mu_d}^\dagger$ , based on Eq. (5) satisfying Fig. 1(g), at site  $l = 0$ . This counting occurs in real time  $t = -i\tau$ , where  $\tau$  is the imaginary time. If the program counter particle is at site  $l$ , then the active CNOT operator  $\mathbf{C}_l$  flipping a spin is at  $|0 \dots \underbrace{1 \dots 0}_{l} \dots 0\rangle \mathbf{C}_l \dots E_{\text{in}}|\Psi(t)\rangle$ .
      - (b) If the particles' final state in  $B$  contains a Hamiltonian component with the counter particle at site  $l \rightarrow \mu_d$ , then the counting is finished. The rate to store the counted spin flips measured in Hz between sites  $l$  and  $l'$ , is  $v_{ll'}\tau$ . The desired Hamiltonian after  $\Delta t^* = tv_{ll'} - s$  steps, as a phase shift parameter, where  $tv_{ll'} = t^*$ , is projected out as
$$E_{\text{out}}^s |0\dots 01\rangle\Psi(\tau) = \mathbf{C}_{\mu_d} \mathbf{C}_{\mu_d-1} \dots \mathbf{C}_1 E_{\text{in}}^{\Delta t^*} \Psi(t) = \mathbf{c}_{\mu_d}^\dagger \mathbf{c}_{\mu_d} e^{-\beta_\tau E} |10\dots 0\rangle\Psi(t), \quad s \in \mathbb{Z}^+, \quad (22)$$
where the number of counter particles is a constant  $\sum_{l=0}^{\mu_d} \mathbf{c}_l^\dagger \mathbf{c}_l$ ,  $\mathbf{c}$  is an untrapped particle, and  $\beta_\tau = \tau/\hbar$  is the length of the  $\tau$  interval [25, 40, 41], where  $\hbar$  is the Dirac constant. Also see Eqs. (23)–(29).
  - 3: Decompress gradually from the degenerate ground states in the superdense code to classical states using a combination of our system communication model, Ionicioiu and Wang *et al.*'s models [40, 44, 52, 79].
    - (a) The compressed code is based on the cat state method, e.g. [44], and pairwise site BEC atoms with a product state from step 1(a).
    - (b) The compressed quantum code can be decoded to classical bits by implementing CNOT logic [40]. All outputs are reversible to a set of classical or quantum states by inspecting the input states and the CNOT output using a photoprobe (see [2, 3] code examples).
- 

returning  $E'_{\text{out}} \Phi$ . From Def. 5 and Algorithm 1 steps 2–4,  $|\Psi\rangle_{AB} = \frac{1}{\sqrt{2}}(|1\boxed{11}\boxed{1} + |0\boxed{00}\boxed{0}\rangle)$ . Thus,  $\rho_B = \text{tr}_A \rho = \frac{1}{2}(|11\rangle_{23}\langle 11|_{23} + |00\rangle_{23}\langle 00|_{23}) = \frac{1}{2}[\begin{smallmatrix} 1 & 0 \\ 0 & 1 \end{smallmatrix}]$  with entropy  $S(\rho_B) = \log 2$  denotes a maximally entangled state.

**Remark 5.** In Example 3, the corresponding basis of a 4-qubit register can be initialized and mapped using pairwise Pauli-X and Hadamard gates (compare to, qubit pairs in entangling gates [54]). From there, the basis of the two-qubit register can be represented by a CNOT gate in Hadamard transformed basis, and measured accordingly. The subcircuit code is presented in [3, Meth. Valid. I].

In Example 3, for a number of photoprobes encoding  $2n$  states (or  $n$  qubits) due to particle pairwising from Sec. 4, there is at least one pair entangled, and a photoprobe

superposed. Thus, maximum entanglement is observed between particles with entropy  $S(\rho_B) = S(\rho_A) = n \log 2$  (Example 1). In this case, Schrödinger's cat state [16] is the most probable outcome as  $h \in (0, 1]$ , which is the external magnetic strength between the inside area sites of quadrants 2 and 3 entangled with area sites 1 and 4. This is subject to EE scaling as follows.

## 7. Entanglement scaling

The entanglement scaling behaviour in the heat engine is determined by measuring the Hamiltonian, whereas its dimensions are based on the heat engine space describing particle interaction, energy exchange and spins.

## 7.1. The Hamiltonian and EE scaling

From Def. 5, Examples 2 and 3, EE is ideal for determining entanglement between lattice sites where QPTs occur [57, 77]. This entropy as a function of the inside area with  $D$ -spatial dimensions, asymptotically scales as  $S_L \sim L^{D-1}$ . For example,  $N$  atoms occupy a 2D-array of  $L^2$  lattice sites. Its entropy  $S_L = S(L)$  is measured by observing any exceptions to EE's *area law* [19, Appdx. F], which holds for all gapped ground states on a 1D lattice [77, 78, 109]. This is followed by a  $\log L^{D-1}/3$  added to the strength  $J$  of a spin-spin interaction in the Hamiltonian

$$H = -J \sum_{\langle II' \rangle} \sigma_l^z \sigma_{l'}^z - h \sum_l \sigma_l^x, \quad (23)$$

where  $\sigma$  is the spin configuration (spin up +1 or spin down -1) as an assignment of spin value to site  $l$  or  $l'$ , from the expected loci  $\langle \ell \ell' \rangle$ , where a spin flipping event  $i$  or  $j$  occurs in the  $z$ -direction [67]. The Hamiltonian corresponds to a non-critical spin chain, where its values are plotted in Fig. 5(a), saturating to a constant (area law) [77]. This energy has the periodic boundary conditions  $\sigma_{\mu_d+1}^z = \sigma_1^z$ , i.e., a finite number of spins on a 1D ring as part of the CNT layer.

The energy readout is based on the program counter particle [40] that moves from site-to-site using operator  $C_s$ , which acts on register qubits (Algorithm 2). The Ising model experiences a PT between an ordered and disordered regime at  $J \sim h$ . This is where  $h$  is applied to lattice sites, and  $J$  as the interaction strength between the closest pair of particles (sites), is used to evaluate a critical behaviour. For a quantum critical spin chain,  $S_L$  diverges logarithmically.

From the BEC EPR pair teleportation model [65, 66], for step 2 of Algorithm 2, applying a spin operation to the area  $\langle II' \rangle$  where the beam splitter interacts, a BEC is split into a BEC pair [65, 66]. For the BEC pair, as shown in Fig. 3(d), the effective interaction Hamiltonian scaled from Eq. (23), as the potential part is

$$H = (\sigma_l^z + \sigma_{l'}^z)^2 = (\sigma_l^z)^2 + (\sigma_{l'}^z)^2 + 2\sigma_l^z \sigma_{l'}^z, \quad (24)$$

where applying the  $\sigma_l^z \sigma_{l'}^z$  operation to two  $\sigma^x$ -polarized BECs, corresponds to an entangling Hamiltonian between two traps (or XX-gates e.g., [54]), one at  $l$ , entangled with the other at  $l'$ , as simulated in [3], or see Appx. A. This is a correlated system of BEC EPR pairs [65, 66], see Example 2.B. A Bell correlations sum of  $(2, 2\sqrt{2})$ , [1, Eq. (18)], is predicted from the QDF as  $|\langle \mathbf{k}r \rangle| \rightarrow 1$  between the two entangled states  $|i_{II'} j_{II'}\rangle$ , for which by Eqs. (6)–(18), have the variances  $\Delta(\mathbf{k}_{i,j})_{II'} \rightarrow 0$  and  $\Delta(\mathbf{r}_{i_{II'}} + \mathbf{r}_{j_{II'}}) \rightarrow 0$ , [64, Sec. 6]. This denotes there is a minimum to no variation in the observables of the EPR pair, once entangled across the interval  $\Delta t^*$ , where  $|\langle \mathfrak{P} \rangle| \rightarrow 2$  under a QDF transformation, see Figs. 2 and 3(b).

The inverse of the BEC EPR teleportation is superdense coding in Algorithm 2, step 3: the EPR resource is shared as the BEC EPR state over a quantum channel to decode the system's quantum state in classical bits.

## 7.2. System's total energy conditions

There are two total energy conditions of the system which apply to Eq. (23). These energy conditions can be derived from any PT via scalar  $\kappa$  field products from Eq. (19) [1], relative to Eq. (22). The expected energy conditions observed from the quantum energy conservation [82–84, 89, 104, 108], are as follows:

$$|E\langle f(\kappa)\ell \rangle| = \begin{cases} H\Psi = E\Psi, & \text{as } H = E = \text{const.}, \\ H\Psi \neq E\Psi, & \text{as } E_{\text{in}}^{\Delta t^*}\Psi(t) \mapsto E_{\text{out}}^s\Psi(\tau), \end{cases} \quad (25)$$

where the first condition  $H\Psi = E\Psi$  is valid for the total energy  $E = H$  being conserved, which is constant in the classical and quantum oscillation models (e.g., Ising), and time-independent. The second condition  $H\Psi \neq E\Psi$  is valid under the Wick rotation  $-i\tau = t \mapsto \tau$ , corresponding to the thermodynamic events observed from the contour integral [25, 41], Fig. 4. The scalar operation in the second condition conserves  $E$  quantitatively for  $H$  due to a physical fact about systems  $A$  and  $B$  to contain time. This is based on particle entanglement independent of coordinate choices made on  $\mathbf{k}$  and  $\mathbf{r}$  between pairwise particles communicating within  $AB$ . This condition also applies to a non-equilibrium state that can be extrapolated (recording all QDF data via QAI) from a cooling process (BEC) in this system [25, 85].

The QDF scalar behaviour occurs from the scalar QDF operation from Def. 1 and Eq. (15). This is due to a planewave travel along  $\mathbf{k}$  by the photoprobe projecting its state onto the state of a particle pair. As presented in Sec. 3, the particle pair can be in a lattice, or entangled between sites as demarcated between Figs. 1(a) and 1(d).

An inverse correlation between field components  $\mathbf{k}$  and  $\mathbf{r}$  is expected under a  $\kappa$ -based QDF transformation from Eq. (15), as  $|\mathbf{k}| = 2\pi\lambda_c^{-1} \rightarrow \infty$ , and  $|\mathbf{r}|$  tends to  $\lambda_p$ , where  $\lambda_c \rightarrow \lambda_p$  [74–76]. This denotes a photoprobe travelling across a distance of  $2|\langle f(\kappa)\ell \rangle|r \rightarrow \lambda_p$  between two field points, Eqs. (8)–(14), relative to its interacting particle at distance  $|\mathbf{r}| \rightarrow \lambda_p$  within system  $B$ . This is a quantum particle in a ground state, Sec. 4.1 [1, Sec. 5].

The photon propagator between lattice sites in system  $B$ , Fig. 1(g), propagates the quantum state of a particle from one of the lattice sites (of the 4-qubit register) to system  $A$ , which can assume  $e^{-\beta_\tau H}$  between those sites, Eq. (23). This propagation occurs between the energy input phase and output phase, as discussed in Example 3. The propagator

$$|\Psi(t)\rangle \mapsto |\Psi(\tau)\rangle = \langle \Psi(\tau)|e^{-\beta_\tau H}|\Psi(t)\rangle \quad (26)$$

satisfies  $E_{\text{in}}^{\Delta t^*}\Psi(t) = E_{\text{out}}^s\Psi(\tau)$  under the Wick rotation from Eq. (25). In our model, however, the condition  $H\Psi = E\Psi$  applies to Eq. (23) as a bi-directional QDF, where one direction is, e.g., Eq. (16).

## 7.3. Probability measure in EE scaling

Figure 5(b) shows  $\lambda_c$  for non-critical phenomena translating to a finite entanglement length  $L_E$ . This length has a value of  $L$  for which adding new spins to a block does not increase its entanglement with the rest of the chain. As in

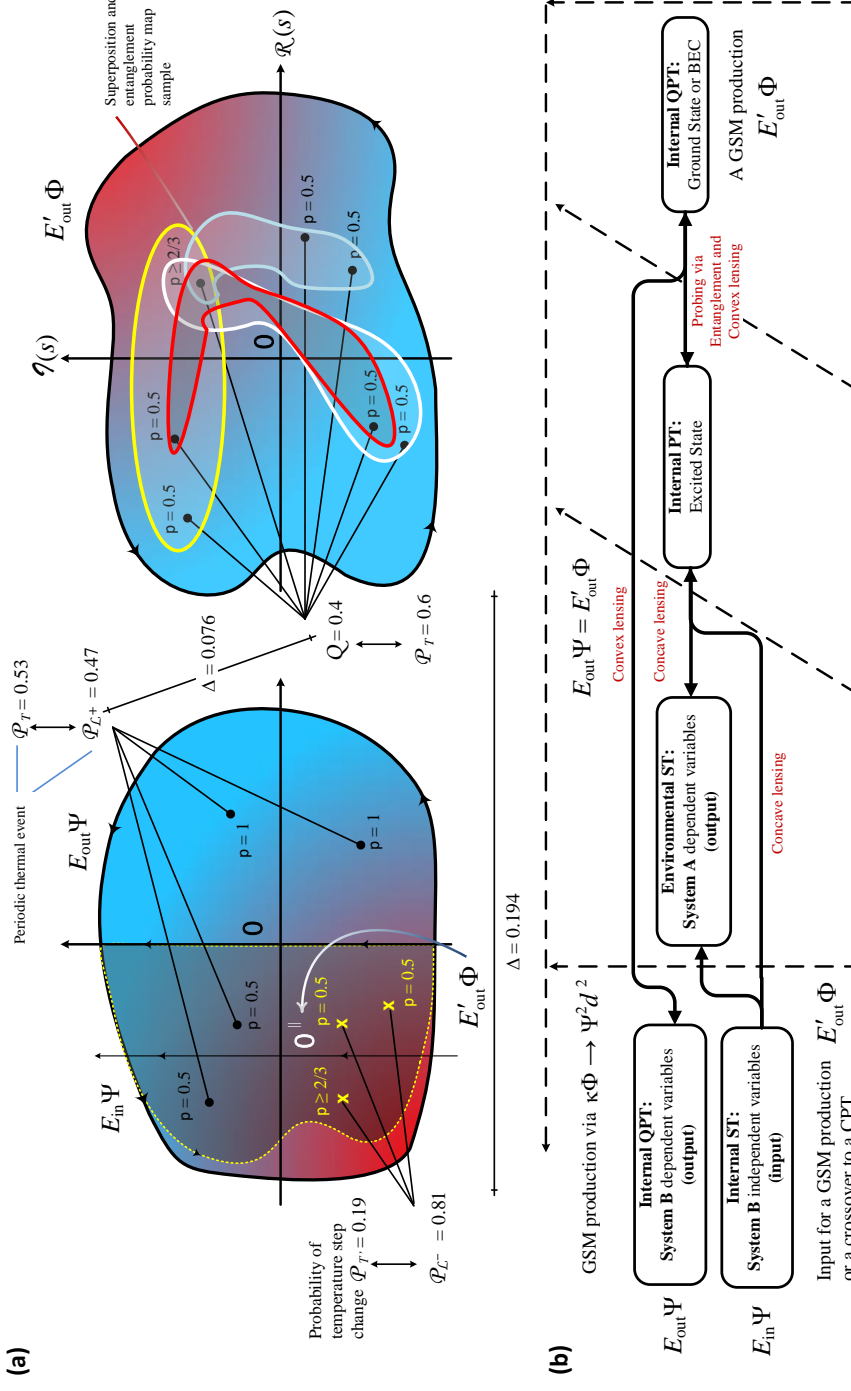


**Fig. 4.** **(a)** A DFC example to simulate a lens input-output product from the proposed system, Fig. 1. Internal system  $B$  (leftmost) equipped with lenses, after sampling from the external system  $A$  (right-to-left), projects and distributes particle states. This is shown by a particle superposing between the input side and output side, with a  $p = 0.5$ . A GSM production is shown as a QPT against an internal PT in  $B$  (left-to-right). **(b)** The periodic thermal event flow (system energy path, 1st objective in Sec. 2) maps the  $p$ 's of a spin flipping event in  $\mathcal{O}^\parallel$  to  $\mathcal{O}$  via entanglement, and to convex coding areas between the  $p$ 's within the quadrants. The dotted arrows cover and point to the quadrants where the flow carries the expected lens products relative to a temperature step. The flow direction favours the expected system state in **(a)**. **(a, b)** Each quadrant has a probability sum of 1 over one or more events as the magnitude of their occurrence (frequency), Eq. (32). This probability sum falls on the same axes' side. The coding areas for a greater magnitude of events across the quadrants denote superposition or entanglement, and have different colors to distinguish between system temperature steps by measuring probabilities  $P_T$  and  $P_{T'}$ , Sec. 7.3. The shared value of  $p \geq \frac{2}{3}$  is distributed in system  $B$ , given the ST probability  $\mathcal{P}(\Phi \rightarrow \Psi) \geq \frac{2}{3}$  via  $\kappa$ , which indicates superposition and entanglement between particles in  $A$  and  $B$ . The information about the possibility of entanglement is extracted from the counter particles in  $B$ , with slave Ising spins.

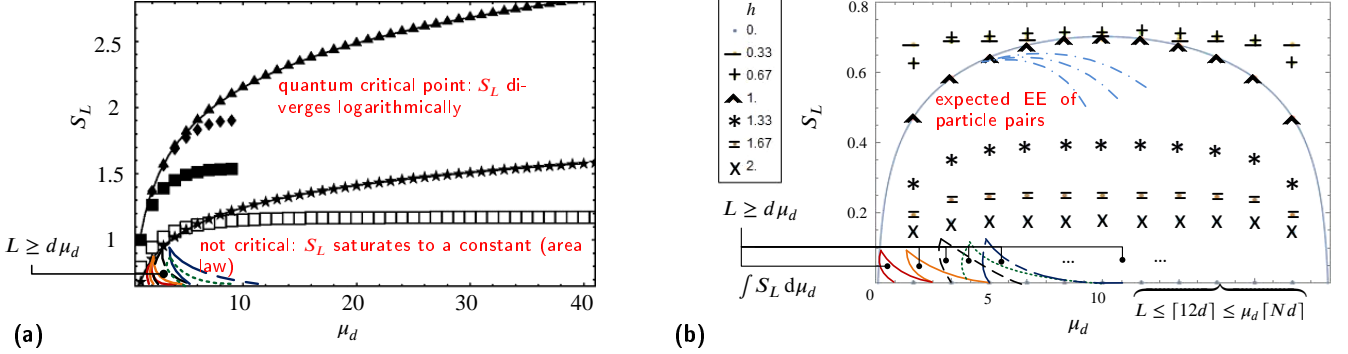


**Fig. 5:** (a) A noncritical Ising chain ( $\square$ ) is with  $J = 1$ , and  $h = 1$ ; noncritical chain ( $\blacksquare$ ), has  $h = 0$ . A critical chain ( $\star$ ) has a log divergence for a large  $L \leq \mu_d [Nd]$ , Eq. (5):  $S_L \sim \log(L)/6$ ; the curve  $S_L \sim \log(L)/3$  ( $\blacktriangle$ ) corresponds to the critical chain with  $h = \infty$ , and  $J = 0$ . A chain of  $N = 20$  spins ( $\blacklozenge$ ) with zero magnetic field, combines critical log behavior, or low  $L$ , with a finite chain saturation effect, asymptotically described by a free boson [43, 57, 58]. (b) Given the QDF transform, non-entangled states conform to the point of entanglement, as entropy is measured for  $L \rightarrow [10d]$ , and decays as  $N \rightarrow \infty$ , i.e., the conformal field theory predicting 2nd and 3rd order PTs (of  $D > 2$ ) [61, 70]. (a) or (b) Sawtooth curves of  $L \in [d\mu_d, \mu_d \lceil Nd \rceil]$  form the area under the  $S_L$  curve by its integral, accounting for EE scaling based on pairwise interactions relative to a DF lens product delivered to a photoprobe at  $d$ , Sec. 4.

the Ising model [42, 43, 58],  $L_{\mathcal{E}}$  diverges at the critical point  $h = 1$ , which is when  $|\mathbf{r}| \rightarrow \lambda_p$  and  $\lambda_c \rightarrow \infty$  in Eq. (15).

As  $h > 0$  (yet,  $h < 1$ ), the GS products  $|0 \dots 0\rangle$  and  $|1 \dots 1\rangle$ , given  $|1, m\rangle = |0, m-1\rangle$  for  $m > 0$  modes, are not fully degenerate due to a splitting of order  $h^N$  between the products  $|\Psi\rangle_{AB} = \frac{1}{\sqrt{2}}(|0 \dots 0\rangle + |1 \dots 1\rangle)$ .

Therefore, the only ground states are Schrödinger's cat state  $|0 \dots 0\rangle$  which is unstable against small perturbations, as  $N \rightarrow \infty$ . This macroscopic superposition gives an extra entanglement of  $\log 2$ , as shown in the plot. If the chain is cut at  $L$  away from the boundary, the shorter piece (limiting the degrees of freedom) denotes entanglement obtaining the  $\log L$  scaling as a function of the cut, which conforms to the results plotted in Fig. 5(a). The measurement from the transverse Ising model [57], scales to one dimension in the outer layer of the CNT, and scales to  $D$  dimensions in the CNT interior (of system  $B$ , Fig. 1). Both layers are in contact with system  $A$ , where entanglement is determined at the point of contact. This is by producing particle interactions between  $A$  and  $B$  with photoprobes followed by their state readout. For the external CNT layer, the Hamiltonian is Eq. (23) with the same boundary conditions. The configuration probability is given by the Boltzmann distribution

$$\mathcal{P} = e^{-\beta H} / Z_\beta, \quad \beta = -i\beta_\tau = 1/k_B T, \quad (27)$$

where  $\beta$  is the system's coldness,  $T$  is the temperature,  $k_B$  is the Boltzmann constant, and

$$Z_\beta = \sum_\sigma e^{-\beta H} = \sum_{\substack{\forall n \geq m \in \\ |i_m i_n\rangle \in f(\kappa) \mathbb{F}}} e^{-\beta E_{|i_m i_n\rangle}}, \quad (28)$$

is the partition function [21, 43, 69, 70], which shows the complete picture of the thermal state of the system through the density matrix of the Hamiltonian,  $\rho_\beta = e^{\beta H}$ . For

example, the GS and ES based on states  $|i_m\rangle$  and  $|i_n\rangle$  in a QDF transformation (a PT switch) can be determined between  $l$  and  $l'$  sites as the states propagate in real time, Eqs. (22)–(26). The desired Hamiltonian can be encoded into a QDF matrix within the lens coding circuit (Algorithm 2), [3]. This is done by using energy operators, the *kinetic* and *potential interactions* between particles [97].

The system via such interactions is set to thermalize (an equilibrium) to an inverse temperature, given the system's energy and periodic boundary conditions from Eqs. (23)–(25). This denotes  $\rho_\beta$  is tied to the time-evolution operator or propagator  $e^{-\beta_\tau H}$  from Eq. (26) by setting  $\beta \mapsto -\beta_\tau$ . This further shows the system evolves in imaginary time while diffusing in real time  $t = \tau\tau$ . The diffusion is observed by linking the quantum mechanical at  $T = 0$  (or GS) via  $\kappa$ -based QDF of spacetime ( $D-1\beta_\tau$ , to a classical at  $T = k_B\beta \geq T_c$  in a  $D-1$  dimensional space, Fig. 3. Hence, a CPT or QPT per switch, Eq. (11), can be determined by computing  $\mathcal{P}$ , which is based on a spin flip or an average of spins flipping in system  $A$  relative to spins flipping in the CNT layer of system  $B$ . That is to ask, which lattice sites are more ferromagnetic (aligned spins) against their neighboring sites in an ordered or disordered state of the system?

Figure 4(b) shows the periodic boundary condition of spin assignments to the CNT layer (lattice sites) and the environment, as an example of events that might occur in systems  $A$  and  $B$ . The probability of each temperature step between these systems is the expected result from Eq. (27). This is computed based on the inverse of temperature in Eq. (27), on the imaginary (time) axis  $l(s)$  relative to the real axis  $R(s)$  of the periodic boundary [69], as shown in Fig. 4(a). The description of the Hamiltonian for this behaviour is researched and simulated by Haas *et al.* [77], proving a

*spinless fermion* or a *boson-like net spin* that will satisfy the  $\Phi$  component of the QDF,  $\langle \Psi \Phi \rangle$  in our system.

The photoprobes read out the atomic spin states (of the field  $\Psi$ ) to see if a spin is up or down. A prediction interval satisfying a future readout value falls within the range of possible probabilities  $> \frac{2}{3}$ , given  $h$  and  $J$ , due to superposition between sites relative to the central charge [70]. The probability range is satisfied by implementing  $\kappa$  to transform a field, having its states entangled within a QDF. Here, the interior of the CNT (in  $B$ ) interacts with system  $A$  particles, after the particles in the CNT outer layer interact with the sampled particles from  $A$ . This gives a build-up of  $J$  in a sum form. The lowest to the highest energy state, based on  $2sJ$  between lattice sites from Eq. (23), is additive in the number of flips recorded by counter particles, Eq. (22). The  $p$  of having a spin-flip at each site is independent. The probability ratio of finding a flip, as the  $p$ , to the probability of not finding one, as  $p' = 1 - p$ , is the Boltzmann factor

$$e^{-2\beta sJ} = p/p', \text{ given } \mathcal{P}/\mathcal{P}' = e^{-\beta \Delta E}, \quad (29)$$

where  $\mathcal{P}' = Z_\beta^{-1}$  is the probability of a GSM spin configuration assignment to the sites, and  $\Delta E = E_{\text{out}}^s - E_{\text{in}}^{\Delta t^*} \leq E_{\text{out}}'$  is the energy interval denoting the system's ST, Eq. (12). The probabilities  $p$  and  $p'$  are, respectively, measured for  $\mathcal{P}$  and  $\mathcal{P}'$ , that contribute to the temperature step probabilities  $\mathcal{P}_T = 1 - \mathcal{P}_{\mathfrak{L}^+}$  and  $\mathcal{P}_{T'} = 1 - \mathcal{P}_{\mathfrak{L}^-}$ . The probability  $\mathcal{P}_T$  denotes a temperature change towards an ES by applying  $\mathfrak{L}^-$  with a probability of not having a convex product in system  $A$ . The probability  $\mathcal{P}_{T'}$  denotes a temperature change towards a GS by applying  $\mathfrak{L}^+$  with a probability of not having a concave product in system  $B$ . This change is due to the change in the average spin of particles in each site as a thermal event, that can result in a PT. The spin flips are recorded by the adder (Algorithm 2), where Fig. 4(a) shows an example of  $p$ 's of spin flips, given the spin configuration of each site across the energy surface.

#### 7.4. Code for an EE computation

A strong prediction (probabilities of  $> 2/3$ ), Eq. (29), can be made based on entanglement by a QDF transformation. This transformation is determined for any particle interacting with another causing a spin flip. Under superconductivity conditions, Sec. 3, [57, 61], and the beam splitter operation from Example 2.B, a block of flipped spins can result in entangled particle pairs. The distance between entanglement points can be measured relative to  $\lambda_p$  where the pairs contribute their energy after  $\Delta t^*$  steps to a PT, Eqs. (15), (22)–(26), and Fig. 5. The boundary conditions of EE scaling prior to an entanglement measure can be defined by implementing the following steps in an EE coding model [3].

1. Apply a 1D Ising model to the external CNT by having the Hamiltonian to compute EE, and see if any particles in  $A$  and  $B$  are entangled.
2. Apply a 2D Ising model to  $D$ -dimensional sites from e.g., the CNT interior for determining entanglement using photoprobes from the  $\Phi$  field. Scalar  $\kappa$  transforms the field to a  $\Psi$  field for accurate readouts of

atomic states. The prediction of spin flips to determine the system state is based on Eq. (29).

3. Write a DF code based on the coding steps in Algorithm 2 and Example 3, satisfying qubit compression and decompression. A classical state is extracted from the Schrödinger's cat state based on the last two step predictions from a photoprobe readout. Entanglement with an expected probability  $\approx 1$  is extracted from the readout prior to its occurrence per spin flip.  
–⊗ The measurement of a cat state giving extra entanglement is presented in [3]. This is shown in Figs. 5(a, b) as an expected event between the SWCNT and the CNT interior, Figs. 1(d, f).  
–⊗ The input denoting entanglement is a black dot in Fig. 1(g), and the rest of the gates are the inverse (no entanglement or white dots). The photoprobes are later used to decompress the count by reading the state of the trapped particles into classical states. Classical states during quantum decoherence are obtained by a gradual diffusion of BEC at a QPT level, Example 4.
4. Distinguish and classify Bell states [3, Eqs. (25)–(35)] by using an extra physical qubits in Fig. 1(g).
5. Correct any possible qubit flip errors or information loss due to decoherence with the environment by Fig. 1(g) components. The components can encode any product states into an entangled state of  $3[n, 2n \leq N]$  physical qubits from [1, Remark 5] and [3, Eq. (32)] to correct the qubit error [1, 3, 40], or see [3, p. 21].

**Remark 6.** QDF encoding, decoding and compression can be implemented on  $N$ -qubit machines, satisfying the computations required to perform the boundary conditions above, as a QDF circuit implemented in [3].

The following example shows the coding model for determining entanglement in a periodic quantum compression and decompression of particle states.

**Example 4.** The cat state obeys the following coding model of an ST from [1, Sec. 2.2.1]:  $|i\rangle = \{|0\rangle = [1], |1\rangle = [0], |2\rangle = [|i_m\rangle \otimes (|0\rangle + |1\rangle)] \xrightarrow{\mathcal{T}(i)} |i_{II'}\rangle; i_{II'} \leq 2\}$ , given that  $\mathcal{T}(i)$  is the ST operator, satisfying a cat state to undergo a transformation where entangled states are built with orthogonal states between a pair of particles at their pairwise interaction site  $|II'\rangle$ , e.g.,  $|01 + 10\rangle$  [3, pp. 13–16]. An ST for  $|2\rangle$  as  $|0_m\rangle$  occurs within one of the  $m > 0$  modes of the ground state  $|0\rangle$ , where  $i_m < 2$ . This is a QPT which occurs when a set of atoms are in degenerate ground states [1, 40]. An ST for  $|2\rangle$  appearing in any part of the code is treated as a 3rd state for  $m$  sideband levels of  $|0\rangle$ . Accordingly, in the classical case,  $|2\rangle$  turns into  $|1\rangle$  when particles diffuse from the GSM. This is a continuous QPT crossover to a CPT [21, 43]. For entangled states or those qubit states mimicking Bell states without entanglement, the qubits possess orthogonal and nonorthogonal states, where their product takes the form  $|i_m\rangle \otimes |i_n\rangle \otimes |i_{II'}\rangle$  product states [3]. This is used in the QDF game and circuit models to represent two bits of information that are hidden, and with

an extra qubit in state  $|2\rangle$ ,  $|i_m\rangle|i_n\rangle|i_{l'}\rangle \otimes |2\rangle$ , reveals the information, as discussed in [3, Eqs. (25)–(27)]. Site  $l$ , from Eq. (22), can carry a state of an atom that can be flipped or remain in state  $|2\rangle$ . The inside area of condensate in one of the systems has two sites paired in the  $s$ -based (stepwise) area expressed by  $ll' = l_s l_s + (2s + 1)$ . The area's center has sites  $l_0=0$  and  $l_0+1$ , and the outer center has two sites  $l_1 = l_0 - 1$  and  $l_1 + 3 = l_0 + 2$ , and so on. The compressed code can appear as the representation of a product state for a set of BEC atoms in the interaction area of pairwise sites

$$E_{\text{out}}^s |i_{ll'}\rangle \Psi(\tau) = E_{\text{in}}^{\Delta t^*} \frac{(\mathbf{c}_l^\dagger)^{ll'}}{\sqrt{ll'!}} |2 \dots \underbrace{[2 \ 2 \ 2]}_{l_1 l_1 + 3} \dots 2\rangle \Psi(t), \quad (30)$$

where  $[2 \ 2] = l_0 l_0 + 1$ .

In the code, the possible combination of states is  $2^3$  for a pairwise site where particles could entangle. This is denoted by the product state  $|22\rangle$  which could be  $\{00, 01, 11, 10\}$  with a probability of 1 out of 4 pairs being entangled. To decompress the code as a semiclassical approach, the cat state each time is put into a step-by-step loop, leading to a less condensate. This gives a change in entropy  $S(\rho_B) = n \log 3 \xrightarrow{\Delta t^*} 0 = S(\rho_A)$ , Examples 1–3, which satisfies the first condition in Eq. (25) as a reversible thermodynamic process (arrow of time via QAI [3, 92, 100, 109]). The cat state can be expressed in a density matrix  $\rho_A = \text{tr} \rho_B$  where condensate occurs inside system  $B$  sites. The cat state leading to a loop of gradual diffusion of the GSM is based on tracing the product state after a CNOT gate operation from

$$\begin{aligned} \rho_A^s = & (\dots |02\rangle_{l_0 l_0 + 1} \langle 02|_{l_0 l_0 + 1} + |22\rangle_{l_1 l_0 + 2} \langle 22|_{l_1 l_0 + 2} \\ & + |01\rangle_{l_2 l_0 + 3} \langle 01|_{l_2 l_0 + 3} \dots) \left[ 3ll'! 4 \xrightarrow{\Delta t^*} 4ll'! \right]^{-1}. \end{aligned} \quad (31)$$

Here, a state is diffused from a pure state  $|0\rangle$  relative to  $\Delta t^*$ , as a classical of two or more states. The second element of the trace of the compressed code still needs decoding, as product  $|22\rangle \rightarrow |2\rangle$ , which can be 0 or 1. The final decoded sequence must be distinct, 0 or 1 from a probe readout using scalar  $\kappa$  applied to the particle field of each site. As in Grover's algorithm [16, 26, 40], the number of times the diffusion of states from a GSM can be mapped to the Grover iteration and its diffusion operator. In the lens decoding process, the operator operates on the demarcated areas of pairwise qubits in Eq. (31), ranging from  $\sqrt{2}$  to  $\sqrt{N}$  iterations for a search to obtain a classical state. Here, the GSM is the target for delivering a classical product state to a probe and predict a PT.

**Remark 7.** Any PT crossover from QPT  $\leftrightarrow$  CPT in Example 4, is satisfied by  $\mathcal{T}(i)$ , which can map to the relevant unitary phase shift operators presented in a QDF circuit, e.g., the phase shift measurement of  $\omega_{|i_m\rangle}$  for state  $|i\rangle$  in [3, Meth. Valid. I]. Hereon,  $\mathcal{T}(i)$  is self-contained in most equations due to its repeated use in [1], and only limited to phase shift discussions made in the coding part of the QDF in [3].

**Remark 8.** In Example 4, the values of  $i$  and  $j$  are limited to  $j(j \leq i) \in [0, 2]$ , where the value 2 denotes any GS or ES of a particle's quantum state  $\{|0\rangle, |1\rangle, \dots, |N-1\rangle\} \mapsto |2\rangle$ . This determines a QPT or its crossover PT.

## 8. DF lens products and analysis

To simulate events and analyze results, we plug in the following assumptions to the Mathematica simulator [101].

### 8.1. Lens product assumptions

**Assumption 1.** The concave lens function  $\mathfrak{L}^-$  can produce maximally entangled (two-qubit Bell) states in the system (Examples 1 and 4) if the conditions of producing a GSM and its entanglement are met via e.g., convex lens coding.

This is where the conditions of the experiment meet entangled states, and the measurement is conducted on the periodic events of the system, as illustrated in Fig. 4. The lens distance is short between particles that are in a BEC state, or long when far and scattered through diffusion. Both outcomes can be denoted by a concave, convex, or a sequence of convex-concave, concave-convex products. This is shown in Example 2. Example 3 introduces a QF-LCA and a CNOT gate where  $E_{\text{in}} \Psi$  and  $E_{\text{out}} \Psi$  states are recorded. A lens product is observed, given the following assumptions:

**Assumption 2.** The probabilities of spin-flipping events by particles in ES and GS, Fig. 4(a), represent the same qubits from the above-mentioned examples.

**Assumption 3.** From Def. 4, let a trial by a Laplace transform in the system generate a set of output states in three observable quadrants of energy surface  $\mathcal{O}_q = \{\mathcal{O}_1, \mathcal{O}_2, \mathcal{O}_4\}$ .

**Assumption 4.** Consider Assumptions 1–3. Assume the  $p$ 's from Eq. (29) in form of a sum satisfy  $\mathcal{P}$  in Eq. (27), and contribute to  $\mathcal{P}_T$  or  $\mathcal{P}_{T'}$  measured via the lenses' work done across points of the energy surfaces  $\mathcal{O}_q$  and  $\mathcal{O}_q^{\parallel}$ . The probability of a spin-flipping event squared is  $p_q^2$ , and the probability of its complement is  $p_q'^2$ . These events occur in at least one particle site paired with another in system  $B$ ,  $A$  or between  $A$  and  $B$  as a quantum event.

**Assumption 5.** Assume the density matrices from Examples 2–4 are reused to generate lens products.

### 8.2. Event frequency

From Assumptions 2–5, two events can mutually occur in quadrants  $\mathcal{O}_1$  and  $\mathcal{O}_4$ . The magnitude of events (frequency) on the complex and real sides of the contour (energy path) can give two possible output states

$$\begin{aligned} |j|^2 = & |f(o_1, o_4)|^2 = (p_1 + ip'_1)(p_1 - ip'_1) + \\ & (p_4 + ip'_4)(p_4 - ip'_4) = p_1^2 + p_1'^2 + p_4^2 + p_4'^2 = 2. \end{aligned} \quad (32)$$

Out of the four quadrants, *mutually inclusive* (concurrent) events have the probability  $p_1 \frac{1}{4} + p_4 \frac{4}{4} - (p_1 \frac{1}{4} \times p_4 \frac{4}{4}) = 1$ . Either event is a thermal event of system  $A$  as an ST of an

ES or a GS. In  $\mathcal{O}_2$ , another two events give an output state as the input for  $\mathcal{O}_1^{\parallel}$  and  $\mathcal{O}_2^{\parallel}$ , which is

$$|j|^2 = |f(o_2)|^2 = p_{21}^2 + p_{21}'^2 + p_{22}^2 + p_{22}'^2 = 1. \quad (33)$$

These events have the probability  $p_{21}\frac{1}{8} + p_{22}\frac{2}{8} - (p_{21}\frac{1}{8} \times p_{22}\frac{2}{8}) = 0.53$  for a GSM, superposed or entangled, that contributes to a thermal event (a PT due to change in temperature) from system  $B$  to  $A$ . These events can occur in a total of 8 quadrants: 4 parallel subquadrants of  $\mathcal{O}$  (quadrants of  $\mathcal{O}^{\parallel}$ ) in  $B$ , and 4 quadrants of  $\mathcal{O}$  in  $A$ , Fig. 4(a).

### 8.3. Convex and convex-concave lens products

An energy surface contour integration satisfying a Laplace transform [69] can be used for the continuation of the output state  $o$  in Eqs. (32) and (33), mapping from  $A$  to  $B$  and vice versa. This state continuation can be observed from  $\mathcal{O}_q$  to  $\mathcal{O}_q^{\parallel}$  by the convex lens function

$$\begin{aligned} \mathfrak{L}^+(N) &= \left( \frac{E'_{\text{out}} \Phi - E_{\text{in}} \Psi}{E_{\text{out}} \Psi} \right) \xrightarrow{\text{convex}} \left( 1 - \frac{\mathcal{O}_q}{\mathcal{O}_q^{\parallel}} \right) \\ &\quad \overbrace{\int_1^2 \int_1^3 \approx \frac{2}{3}} \\ &= 1 - \oint_B \frac{dj do}{|j|^2} \quad (34) \\ &= \left( 1 - \lim_{|\mathbf{kr}| \xrightarrow{\kappa} 1} \frac{c}{|\mathbf{kr}|} \int_{\frac{1}{2\pi}}^{2\pi} \int_0^{\frac{1}{ct}} \frac{1}{e^{2\mathbf{kr}}} dk dt \right) \in \left[ \frac{1}{3}, \frac{1}{2} \right], \end{aligned}$$

where  $c$  is measured relative to the projected velocities of particles, given  $|\mathbf{kr}| \rightarrow 1$  via  $\kappa$  satisfies a QDF transformation, Eq. (15), within system  $B$ . Convex lensing  $\mathfrak{L}^+$  on  $N$  particles via symbol  $\rightsquigarrow \blacktriangleright$ , denotes ‘projects onto’ one or more quadrants of the energy surface from the lens. In this case, “projects onto the closed surface inside system  $B$ ,  $\oint_B$ , when the slit is closed,” Fig. 1(b). The opposite is the input state from system  $A$  after particle sampling, Fig. 1(a). The period  $t = 1/2\pi$  defines the frequency component of  $k = |\mathbf{k}| \rightarrow 1/ct$  as the frequency distribution of states across surface  $\mathcal{O}$ , Fig. 4(a), independent of the contour flow direction under the lens function. The choice of the wave propagation factor  $e^{-2\mathbf{kr}}$  (without the  $i$ ) formed after the scattering factor  $e^{i\mathbf{k}_{ij}\mathbf{r}} \rightarrow e^{i\mathbf{kr}}$  in Eq. (8), is to satisfy the integration of photons in  $\mathbf{k}$ -space projecting onto Fig. 4(a) left and right sides (a product of systems  $A$  and  $B$  field interaction). The interval  $\left[ \frac{1}{3}, \frac{1}{2} \right]$  shows that the lens projected onto a quadrant of  $\mathcal{O}$ , and caused the distribution of states across three quadrants of  $\mathcal{O}^{\parallel}$ , returning a convex product. We choose the value  $\frac{1}{3}$  as the shared result for the continuation of  $o$  in  $\mathcal{O}^{\parallel}$ , which is a convex-concave product via  $\mathfrak{L}^-(N)$ . To locate the position of the convex product (or its continuation) from the point of origin in  $\mathcal{O}$ , is to compute the modulus of  $r_{\mathfrak{L}^+}$  ( $r_{\mathfrak{L}^-}$ , if concave) as  $|x|$ . This is the magnitude of a complex number showing where the lens product will possibly emit. This is expressed as  $|x| = |y + zi|$ , where  $z$  is the imaginary part of  $r_{\mathfrak{L}^{\pm}}$  on axis  $I(s)$ , and  $y$  is the

real part on axis  $R(s)$ , together model the wave propagation characteristics [33] ( $\mathbf{k}$  is translated to  $\mathbf{r}$  of the field).

The lens product based on the  $\mathbf{k}$ -space integration in Eq. (34), has a magnitude of  $r_{\mathfrak{L}^{\pm}} = |x| \in (4, 4.5)$ . This magnitude denotes a convex vector direction outside the unit circle boundaries  $r_{\mathfrak{L}^+} \geq 1 + \sqrt{2}$  or  $r_{\mathfrak{L}^+} \leq -1 - \sqrt{2}$ . This denotes the photoprobe wave propagation outwards (a planewave travelling in the  $x$ -direction) into system  $A$  (Fig. 4(a) r.h.s. of the contour), while the wave propagates inwards into system  $B$ 's complex plane. Thus, the wave projects onto the sampled and trapped particle space. To show this, we remove the subtraction from 1 operation in the energy surface ratio component of Eq. (34). As a result, in the equation, the component  $E'_{\text{out}} \Phi$  is ignored. The outcome will conform to the negative axes of  $I(s)$  and  $R(s)$  on the l.h.s. of Fig. 4(a),  $\mathfrak{L}^+(N|e^{-2i}) \approx -1 - 4i$ , with  $r_{\mathfrak{L}^+} \approx 4$ , as the wave propagates in the lower end of the contour. Naturally, by reinstating the subtraction, the outcome conforms to the positive axes of Fig. 4(a) r.h.s., from system  $A$  to  $B$  as  $1 - \mathfrak{L}^+(N|e^{-2i}) \approx 2 + 4i$ , with  $r_{\mathfrak{L}^+} \approx 4.5$ . This proves the photoprobe wave propagates inwards from system  $A$  to  $B$ , with a possibility to entangle with system  $A$  particles. This also shows that  $r_{\mathfrak{L}^{\pm}}$  values as quantum events mutually occur within the quadrants of  $\mathcal{O}^{\parallel}$  and  $\mathcal{O}$ , as in superposition.

The probability for a convex lens product in a QPT is computed when  $i$  is factored into the transformation from Eq. (8),  $\kappa\Phi \rightarrow 2\kappa^{-2}\ell r = \Psi\ell d(\mathbf{r}_{i_{ll'}}, \mathbf{r}_{j_{ll'}})$  in Fig. 4 [1, Sec. 4]. From Eqs. (15)–(20), the product is

$$\begin{aligned} \Psi\Phi &= (\kappa\Phi \rightarrow 2\kappa^{-2}\ell r)|\Phi| \\ &= \lim_{|\mathbf{kr}| \xrightarrow{\kappa} 1} \sqrt{\frac{k}{2\pi}} \int \frac{\psi(\mathbf{r}, t)}{e^{2i\mathbf{kr}}} d\mathbf{r} = \frac{1}{e^{2i\mathbf{kr}}} \sqrt{\frac{2}{\pi}}, \end{aligned} \quad (35)$$

where the integral bounds are between 0 and  $r$  within the quadrants of  $\mathcal{O}^{\parallel}$  for all  $\mathbf{r}$  of this product. This is assuming  $\Phi$  is normalized, so that its integral from  $-\infty$  to  $\infty$  equals 1. The average momentum  $\langle \mathbf{k} \rangle$  is computed from  $\psi(\mathbf{r}, t)$ , as the QDF projects the product onto the complex plane at  $r_{\mathfrak{L}^+} \approx 1$ . This applies to general cases of QPTs occurring in the CNT layer, as the QDF projects from  $B \leftrightarrow A$  space, producing mutually inclusive lensing events in  $\mathcal{O}_q \cap \mathcal{O}_q^{\parallel}$ . There are  $2n \leq N$  photoprobes projecting onto the particle pair space via the convex lens integration around left and right contours in Fig. 4. The propagation factor in Eq. (35) alters to a pairwise particle interaction phase  $e^{-2n\mathbf{kr}} e^{-\Delta N i \mathbf{kr}}$  within the QDF, Eqs. (4)–(17) and (36), where

$$\Delta N = (\mu_{ij} - 2n) \leq \mu_{ij} \quad (36)$$

interactions, according to Eqs. (1)–(5). For a 3D trap, the periodic boundary condition from Sec. 4 satisfying  $|\langle \Phi\Psi \rangle| = 1$  for  $\Phi\Psi^2 \rightarrow |\langle \Phi\Psi \rangle|\Psi = e^{i\mathbf{kr}} \sqrt{L^{-3}}$ , [1], is applied to a three-particle interaction within system  $B$ . That is, the counter and sampled particles in the CNOT gate operation created by a photoprobe. This condition conserves a magnitude of  $r_{\mathfrak{L}^{\pm}} \in (0, 1]$  focused within the quadrants of  $\mathcal{O}^{\parallel}$ . Here, qubits are stored and QF-LCA is trained by classifying and reading out states via photoprobes [3, Meth. Valid. I].

**Table 1**

Upper table:  $|\Delta|$  calculations. Lower table:  $S$  and  $|\Delta\mathfrak{L}_{AB}^\pm|$  results are computed between lensing events through the QDF lens relative to  $\Delta t^*$  as a thermal event, as well as entanglement, given the correlation  $\langle \mathbf{kr} \rangle$  via  $|\Delta|$  and  $d$ .

$f_{ \Delta }$	$\mathcal{Q}_{\mathfrak{L}^+}$	$\mathcal{P}_{\mathfrak{L}^+}$	$\mathcal{P}_{\mathfrak{L}^-}$
$\mathcal{Q}_{\mathfrak{L}^+}$	0	$[0.04, 0.1]$	$[0.22, 0.44]$
$\mathcal{P}_{\mathfrak{L}^+}$	$[0.04, 0.1]$	0	$[0.33, 0.53]$
$\rho$	$\rho_B \xrightarrow{\Delta t^*} \rho_A$	$\rho_A \xrightarrow{\Delta t^*} \rho_B$	$\rho_{AB}$
$S$	$[0, n \log 3]$	$(0, n \log 3]$	$\left(0, \frac{n \log 3}{\log 2}\right]$
$ \Delta\mathfrak{L}_{AB}^\pm $	$\underbrace{\left[0.1, \frac{1}{3}\right] L_\mathcal{E}^{-D}}_{\text{Does not satisfy Eq. (18)}}$	$\underbrace{\left[0.1, \frac{1}{3}\right] L_\mathcal{E}^{-D}}_{\text{Can satisfy Eq. (18) via Ising model}}$	$\underbrace{\left(\frac{1}{2}, 1\right] L_\mathcal{E}^{-D}}_{\text{Satisfies Eqs. (15)–(18) via our model}}$

#### 8.4. Energy distribution of a lens product

From Eqs. (14), (17), (23)–(29), (35), the energy distribution of a set of particles exchanging energy between fields  $\Psi$  and  $\Phi$ , [70], depends on the density of states  $\varrho(E)$  as the distribution function of energy giving the number of states occupied across  $q$  quadrants. This density function via  $\mathfrak{L}^+$  can be simulated in  $s$  steps by computing  $Z_\beta$  from Eq. (28), to determine the average number of spins flipping in the system by  $N - n$  particles. Once  $Z_\beta$  is known, a particle site occupied by the  $n$ th particle in state  $|i_n\rangle$  can be determined based on  $\Delta E$ , Eq. (14). A lens product from  $\varrho(E)$  in  $\mathcal{O}$  can be delivered to the probe for a readout. This is conducted by the projection of the photoprobe field  $\Phi$  from Eq. (35), relative to the average positions of the sampled and counter particles, Eq. (20). This measurement is significant in experimental situations when the mechanical effects of light and its interaction with sampled and trapped particles are observed [40, Chap. 11]. The lens product is

$$\mathfrak{L}^+(\mathcal{O}k) = \overbrace{\varrho(E\lambda_c)\Phi^2}^{\text{BED component}} \overbrace{\varrho(E)^{-2}(\kappa^2\Psi \rightarrow \Phi)^{-2}}^{\text{FDD component}} = \frac{(8\pi E)^2 k^3}{\lambda_c h_P^3 c^3} \left( \frac{4\pi\sqrt{2\mu^3 E}}{h_P^3} \right)^{-2} = \frac{2h_P^3 E}{\lambda_c^4 \mathcal{U}^3 c^3}, \quad (37)$$

where  $h_P$  is the Planck constant, and  $\mathfrak{L}^+(\mathcal{O}k)$  is measured in newtons as the resultant force from photoprobe projections onto the sampled and trapped particle space. As the lensing event frequency increases, the magnitude of the force increases proportionally with a magnitude of  $|j|$ . The inverse square part of Eq. (37), denotes a sampled particle in a trap with mass  $\mathcal{U}$  to have a spin value counted by a counter particle with mass  $\mathcal{U}_c$ , Algorithm 2. This mass is factored out to satisfy the desired Hamiltonian from Eq. (22). The photon energy density is factored into the thermal radiation from the trap within the Bose-Einstein distribution (BED) component relative to the Fermi-Dirac distribution (FDD) component, see e.g., [21]. The thermal radiation from the equipartition theorem [69] denotes the energy amount per unit volume, given the transformation  $\kappa^2\Psi = \kappa^2(e^{i\mathbf{kr}}\sqrt{L^{-3}}) \rightarrow \Phi$ , according to Eqs. (8), (15) and (19).

#### 8.5. Results and analysis

From Eqs. (34)–(37), the measurable density ratio of the DF lens products from system  $B$  to  $A$  is

$$\varrho_{B:A} = \frac{\mathfrak{L}^+(\mathcal{O}k)}{\mathfrak{L}^+(N)q} \lim_{|\mathbf{kr}| \xrightarrow{\kappa} 1} \frac{\kappa^4 \Psi^2 \rightarrow \Phi^2}{2\mathcal{O}e^{2\mathbf{kr}}} \approx \frac{3}{4}, \quad (38)$$

where the value  $2\mathcal{O}$  is due to the QDF formation between systems  $A$  and  $B$ , as  $L^3$  is scaled to  $L_\mathcal{E}$  from Eqs. (23)–(26), or QDF within  $B$  as a BEC EPR pair from Example 2.B, Fig. 3, to determine system  $A$ 's state, steps 1(b)–3 of Algorithm 2. In  $B$ , the parallel quadrants of  $\mathcal{O}_q^{\parallel} = \{\mathcal{O}_3^{\parallel}, \mathcal{O}_4^{\parallel}\}$  are the subquadrants of the macroscale quadrant  $\mathcal{O}_q$ . An energy readout of particles is made by a photoprobe (Sec. 7.4) in these quadrants. Entanglement can occur when the adder Hamiltonian is initialized to the GS, Eq. (31), after the slit is closed per qubit register readout. The slit opens when entanglement is created and determined after interpreting the lens coding data [3]. From there, the rerouting or creation of energy paths is executed. As shown in Fig. 4(a), the minimum probability has a value of  $p \geq \frac{2}{3}$  assigned to the distribution of the probe's state, as well as its superposition. By using quantum lenses, parallel quadrants  $\mathcal{O}_3^{\parallel}$  and  $\mathcal{O}_4^{\parallel}$  give a total of two quantum states as  $3\mathfrak{L}^-$  events. For an outward (macro) projection onto the energy surface  $\mathcal{O}$  reconstructing energy states, assuming the event magnitude  $|j|^2 \in [1.6, 2)$  in the parallel quadrants, the following result is expected

$$\mathfrak{L}^-(N) \xrightarrow{\text{concave}} \left(1 - \frac{\mathcal{O}_q^{\parallel}}{\mathcal{O}_q}\right) = 1 - \frac{c|j|^2}{2|\mathbf{kr}|} \int_{\frac{1}{2\pi}}^{2\pi} \int_0^{\frac{1}{ct}} \frac{1}{e^{2\mathbf{kr}}} dk dt \in [0.4, 0.6]. \quad (39)$$

As  $|\mathbf{kr}| \xrightarrow{\kappa} 1$  from Eq. (15), the more accurate approximation of the events in Fig. 4(a), while if the correlation between  $\mathbf{k}$  and  $\mathbf{r}$  approaches 0 or  $-1$ , any quantum event is nonlocal and outside of the  $AB$  system boundaries. This observation relates to the uncertainty measure of  $\mathbf{k}$  and  $\mathbf{r}$  from [1, 14]. As expressed in Eq. (34), the lens product has a magnitude of  $|\mathfrak{L}^-(N)e^{-2t}| = r_{\mathfrak{L}^-} \approx 4$ . Notably,  $|j|^2$  is measured relative to the sum of all parallel and nonparallel quadrants = 8.

The probability ratio between two event occurrences within quadrants  $\mathcal{O}$  and  $\mathcal{O}^{\parallel}$ , is estimated by the density ratio

$\varrho_{A:B} \geq \frac{1.6}{8}$ . This is relevant to the states that are distributed independently within system  $B$ , and in parallel, distributed to system  $A$ . From Eq. (29) and the cumulative distribution of  $\mathfrak{L}^\pm$  products, a Poisson-Boltzmann distribution of two lens products for a thermal event can be measured, one as convex  $\mathcal{P}_{\mathfrak{L}^+}$ , and the other as concave  $\mathcal{P}_{\mathfrak{L}^-}$ , shown by

$$\begin{aligned}\mathcal{P}_{\mathfrak{L}^+} &= \mathcal{P}\left(\mathfrak{L}^+(N); \varrho_{B:A} = \frac{3}{4}\right) = \sum_{i \in \{0,1\}} \frac{\varrho_{B:A}^i}{e^{\varrho_{B:A} i!}} \in [0.47, 0.8], \\ \mathcal{P}_{\mathfrak{L}^-} &= \mathcal{P}\left(\mathfrak{L}^-(N); \varrho_{A:B} \geq \frac{1.6}{8}\right) = \sum_{i \in \{0,1\}} \frac{\varrho_{A:B}^i}{e^{\varrho_{A:B} i!}} \in [0.8, 1].\end{aligned}\quad (40)$$

The lower bound of the convex probability result shows no thermal event at  $i = 0$ . In case of a thermal event at  $i = 1$ , the upper bound of the interval meets the lower bound of the concave product probability. This denotes a convex product is observed by causing a thermal event, and no concave product causes that same event. However, the upper bound of the concave probability approximates to 1, which is a thermal event caused by a concave product. Thus, the remainder of the distribution (complement) on the lower bounds of both products denotes a thermal event probability  $\mathcal{P}_T = 1 - \mathcal{P}_{\mathfrak{L}^+}|_{i=0} = 0.53$ . This evaluates  $\mathcal{P}_{\mathfrak{L}^+}$  at  $i = 0$  as the probability of distributing a convex product prior to the event. After lensing over  $B$ 's energy surface, in  $A$ ,  $\mathcal{P}_{T'} = 1 - \mathcal{P}_{\mathfrak{L}^-}|_{i=0} = 0.19$  evaluates  $\mathcal{P}_{\mathfrak{L}^-}$  at  $i = 0$  as the probability of distributing a concave product prior to the event. Thus, the maximally entangled states are in the lower bound of the interval shared with the remainder of the  $\mathfrak{L}^+$  cumulative distribution  $\mathfrak{L}^- \cap \mathfrak{L}^+ = 1 - (\mathcal{P}_T + \mathcal{P}_{T'}) = 0.28$ . This estimate is made when a spin system satisfies a thermal event. The cumulative distribution observed by lensing over  $B$ 's energy surface before the concave-convex lensing over  $A$ 's energy surface, as shown in Fig. 4(a), is

$$\mathcal{Q}_{\mathfrak{L}^+} = \mathcal{Q}\left(\mathfrak{L}^+(N); \varrho_{B:A} \geq \frac{3.6}{4}\right) = \sum_{i \in \{0,1\}} \frac{\varrho_{B:A}^i}{e^{\varrho_{B:A} i!}} \in [0.36, 0.76], \quad (41)$$

where the lower bound with a thermal event probability  $\mathcal{P}_T = 0.62$  at  $i = 0$ , has  $\varrho_{B:A} = 1$ . For the upper bound, given  $|j|^2$  at  $i = 1$ , has  $\varrho_{B:A} = (3 + 2/3)/4 \approx 3.6/4$ . The absolute difference  $|\Delta|$  between two lensing events is calculated from the interval bounds of the lens products,  $\mathcal{P}$  and  $\mathcal{Q}$ , or their complements. The result denotes a thermal change, and can be compared to  $\lambda_c$  and  $\lambda_p$  from Eqs. (15)–(18) as the relative magnitude of a lens event and its product

$$|\Delta \mathfrak{L}_{AB}^\pm| = |\Delta| r_{\mathfrak{L}^\pm} / d(r_{\mathfrak{L}^-} \mathfrak{L}^-, r_{\mathfrak{L}^+} \mathfrak{L}^+), \quad (42)$$

which is the difference between the two lensing events in Eqs. (34)–(39). The product magnitude used in  $d$ , Eq. (17), is to scale up the micro-level observation of particle positions to a macro-level observation of the photoprobe wave propagating through one or two lenses around the contours,

and across the energy surfaces. This is to evaluate the QF-LCA, given the thermodynamic metrics and entanglement scaling from Secs. 5–7. The measurement dimensions are scaled to factors of  $\kappa$  as the dimensions of density, Eq. (8). The probability for determining the particle energy state, given  $\langle \mathbf{kr} \rangle$  in  $\langle \Psi \Phi \rangle$ , Eq. (15), can be measured on a micro-level by interpreting the lens coding data. The lens product momenta and (super)position of particles on a macro-level can be measured from  $|\langle \Psi \Phi \rangle|^2$ .

Table 1 lists calculation summary. Function  $f_{|\Delta|}$  takes the row and column values and subtracts them, to see how close the correlation is between thermodynamic parameters as the two distributions of states. The closer the value of  $\Delta$  to 0 (a strong correlation), the closer to a reversible process expected from  $A$  and  $B$  in equilibrium between their two opposing states, i.e., a strong prediction of entanglement [107]. The reversible process from Eq. (25) can be determined by storing qubits denoting EE results in Table 1, given that QF-LCA steps repeat in a QDF circuit. The EE results are evaluated by implementing and observing this circuit in performing a QFT as a  $\kappa$ -based QDF transform, whereas its inverse,  $\text{QFT}^{-1}$ , decodes the qubits. The reversible process is expected after analyzing the output data over a set of QDF transformations observed in the circuit [3, Table 4].

Table 1 bottom row, left column, denotes no entanglement after system  $B$  events, since in Eq. (17), there is  $\mathfrak{L}^+(N) = 0$  convex lensing applied, given  $\mathfrak{L}^-(N) \geq 0.4$  concave lensing, as there is no more particle sampling done. Now consider from the lens product magnitude computed in Eq. (34),  $r_{\mathfrak{L}^+} \approx 4.5$ , and the discussion on altering  $\mathbf{r}_{j_{ll'}}$  to  $L$  in Eq. (17), scaling to  $L_\varepsilon$  in Sec. 7. From Eqs. (17), (34) and (42), we get

$$|\Delta \mathfrak{L}_{AB}^\pm| = 0.04 r_{\mathfrak{L}^+} \left| \frac{l}{3} L^D r_{\mathfrak{L}^+} \right|^{-1} \approx 0.1 L_\varepsilon^{-D}, \quad (43)$$

for the lower bound. The component  $\mathfrak{L}^-(N)$  in  $d$  is 0, and the density ratio conforms to the magnitude of the photoprobe projection onto system  $B$ 's particle space relative to  $A$ . This is based on the assumption of a counter particle being created by the photoprobe travelling across a lens distance equal to  $L^D = \mathbf{r}_{m;j_{ll'}}^2 |\mathbf{r}|^{-1} \geq 1$ , as  $|\mathbf{r}| \rightarrow \lambda_p$ , and  $|\mathbf{r}_{m;j_{ll'}}| \rightarrow 0$  relative to  $\lambda_p$  in Eq. (17). The upper bound returns  $\frac{1}{3} L_\varepsilon^{-D}$  for a possible entanglement between particle pairs. The following paragraphs discuss Eq. (44) accordingly.

Table 1 bottom row, middle column via the Ising model satisfies Algorithm 2 operations using counter particles to count sampled particles in system  $B$ , independent of system  $A$  events, as a classical (deterministic) approach.

Table 1 bottom row, right column, is a mix of upper and lower bounds of three different distributions satisfying Eqs. (15)–(18). The bounds are identified by measuring the average of the lower bounds relative to  $|\mathbf{kr}|$  under a DF transformation due to distributions  $\mathcal{P}_{\mathfrak{L}^\pm}$  and  $\mathcal{Q}_{\mathfrak{L}^+}$  being continuously linked around the contours across systems  $A$  and  $B$  energy surfaces. This returns the bounds for the relative magnitude of the lens product presented in Eq. (44).

$$|\Delta \mathfrak{L}_{AB}^{\pm}| = \begin{cases} \frac{1}{2}(0.22 + 0.33)r_{\mathfrak{L}^+} \left| \left( 0.4r_{\mathfrak{L}^-} - \frac{l}{3}r_{\mathfrak{L}^+} \right) L^D \right|^{-1} > \frac{1}{2}L_{\mathcal{E}}^{-D}, & \text{given } r_{\mathfrak{L}^{\pm}} \approx 4, \\ \frac{1}{2}(0.53 + 0.44)(4) \left| \left( \mathfrak{L}^-(N)4 - \frac{l}{3}4 \right) L^D \right|^{-1} \leq L_{\mathcal{E}}^{-D}, & \text{as } \mathbf{r}_{i,j} \rightarrow \infty, \text{ and } r_{\mathfrak{L}^{\pm}} \approx 4. \end{cases} \quad (44)$$

For either interval,  $r_{\mathfrak{L}^{\pm}} \approx 4$ , and the assumption made is the creation of the counter particles (trap), Eq. (43). For the upper bound, the concave component in  $d$  from Eq. (17) has  $\mathbf{r}_{i,j}$  in the range of  $\lambda_c \rightarrow \infty$ , given  $|\mathbf{k}\mathbf{r}| \rightarrow 1$  under a QDF transformation. In Table 1, the corresponding entropy  $S(\rho_{AB})$  denotes a value for two to three states (determined by  $|i\rangle$  and  $|j\rangle$ , Remark 8) when  $n$  qubits are computed, equivalent to  $n \log_2 3$  of a mixed qubit state.

To list specific entropy results from Table 1, observations on particle sampling must be made as follows.

**Example 5.** From Sec. 3 simulation,  $n$  particles are sampled in  $B$  from  $N$  particles in  $A$ , as  $n \leq N - n$ . If all of the  $n$  particles have spin- $\frac{1}{2}$  in a mixed state, then the average work done by the QDF lens relative to  $\Delta t^*$  is

$$\left\langle \frac{\mathfrak{L}^+(\mathcal{O}k)}{|\Delta \mathfrak{L}_{AB}^{\pm}|} \right\rangle = [n, 2n] \ln(2) k_B T S(\rho_A \| \rho_B \xrightarrow{\Delta t^*} \rho_A),$$

$$\text{where } S(\rho_A \| \rho_B) = -S(\Psi_{AB}) - \text{tr}(\rho_B \log \rho_A) \geq 0, \quad (45)$$

is the quantum relative entropy [106–108] independent of Wick rotations. Notably, from Def. 5 on EE,

$$S(\Psi_{AB}) = S(\rho_A) = -\text{tr}(\rho_A \log \rho_A),$$

where  $\rho_A = \text{tr}_B \rho_{AB}$ , and  $\text{tr}_B$  is the partial trace of a mixed system state  $\rho_{AB}$ . The thermodynamic work done by the QDF lens is directly related to  $S(\rho_A \| \rho_B \xrightarrow{\Delta t^*} \rho_A)$ , which can be used to extrapolate EE under the Wick rotation:

$$S(\Psi_{AB} \xrightarrow{t \mapsto \tau}) = \begin{cases} -[S(\rho_A \| \rho_B) + \text{tr}(\rho_B \log \rho_A)] \\ \xrightarrow{\Delta t^*} S(\rho_A \| \rho_B \xrightarrow{\Delta t^*} \rho_A) \end{cases} \\ = \begin{cases} [S(\rho_B, t \mapsto \tau) & \text{for } E_{\text{in}} \Psi_{BA(t)} \mapsto E_{\text{out}} \Psi_A(\tau) \\ = S(\rho_A, \tau) \leq S(\rho_B, \tau), & ] \\ [S(\rho_A, t \mapsto \tau) & \text{for } E_{\text{in}} \Psi_{AB(t)} \mapsto E_{\text{out}} \Psi_B(\tau) \\ = S(\rho_B, \tau) \leq S(\rho_{AB}, \tau). & ] \end{cases} \quad (46)$$

These two outcomes satisfy the corresponding entropy results in Table 1. As expressed in Eq. (46), the system evolves with time from  $A$  to  $B$  and from  $B$  to  $A$ . This is a cyclic process of the QDF lens producing GSM, entanglement, and an ES, from the energy input side to the energy output side, Fig. 4. Here, the second condition  $H\Psi \neq E\Psi$  from Eq. (25) applies. The first condition  $H\Psi = E\Psi$  is applicable when the QF-LCA is trained by gathering qubit data from qubit registers during gate operations (all reversible). This is based

on weighing and labelling the qubit states as data points in a classifier to predict any entanglement and PT, as a reversible thermodynamic process and lens work. This labelling of the system (spin) Hamiltonian and energy states, [107, 109], is directly related to lens distance label assignments to the classifier after encoding the QDF data. Entanglement is determined on a scale of  $L_{\mathcal{E}}$ , after decoding the QDF data into classical bits, [3]. From Algorithm 2,  $\rho_B$  of  $|\Psi\rangle_{AB}$  can result in maximum entanglement for mixed states, provided that  $S(\rho_B) = S(\rho_A) = n \log 2$ , see Example 3. According to Eq. (31),  $S(\rho_B) = n \log 3 \xrightarrow{\Delta t^*} 0 = S(\rho_A)$ . Hence, the relative entropy from  $\rho_B$  to  $\rho_A$  in  $S(\rho_A \| \rho_B)$  changes to  $\rho_B \xrightarrow{\Delta t^*} \rho_A$  under a Wick rotation, which does not satisfy Eq. (18), nor entanglement in predicting an ST with high probability. In contrast, the reverse  $\rho_A \xrightarrow{\Delta t^*} \rho_B$  satisfies Eq. (18), see Table 1. This shows that although relative entropy is not symmetric, it still can be used to predict the spin Hamiltonian and estimate the uncertainty as the system evolves, Sec. 7.3. From the data obtained on this measurement, the QF-LCA can be trained to make strong predictions [3, Meth. Valid. II].

In this section, the DF lens product analysis did not provide the specific entropy results. However, a comparative analysis was made by the aid of Wolfram|Alpha calculator and Mathematica analysis toolkit [101]. This was conducted between values based on the given density of states. From the micro-level examples, quantum states were distributed and observed on a macro-level as a temperature step, a PT or entanglement from a QPT between systems  $A$  and  $B$ , or within  $B$  as BEC EPR pairs. A PT can then be predicted by decoding the compressed data on  $2n$  qubits.

The implementation of QF-LCA on quantum computers, IBMQE and QI is provided in our method article [3] associated with this paper. The method article includes a quantum classification scheme using research [98, 99] for tracking and training data points to predict a system state or measurement outcome from a QDF circuit. This involves distinguishability of Bell states and EPR pairs as discussed in [1], simulated and implemented in the method article.

## 9. Conclusion

In this paper, a double-field computation (DFC) model to simulate physical systems is proposed, which mimics observations on particle states and their distribution as lens products, which are delivered through quantum lenses. The products come from the micro-observables, e.g., particles interacting via a DF as a quantum DF (QDF) lens in a quantum phase transition (QPT). The system is split into  $A$

and  $B$ , where  $A$  has particles sampled by  $B$  as a heat engine to satisfy a quantum measurement. This measurement is observed by simulating counter particles that are created by photopropes, given the energy level change of atoms within  $B$ 's physical media. The proposed simulated system by DFC has carbon nanotubes (CNTs) or alternatively, boron nitride nanotubes (BNTs), obeying the Ising model, and (super)conductors to manifest entanglement contained within the QDF using DF lenses that distribute particle states between  $A$  and  $B$ . In this simulation, photopropes are generated from the CNTs as photons in their probe field projected onto atomic sites from  $A$ , where atoms are sampled and processed in  $B$ . Photodetectors gather information from photons that are re-emitted from the atoms to determine their states, prior to a QPT or a classical PT (CPT).

A macro analysis of the observable particle states was conducted by simulating the distribution of states as lens products, which were projected from one or more lenses over a lens distance as a metric. This included simulating an energy surface contour model to show the magnitude of events, given the lens distance on a micro-level from our lens coding examples. From the lens coding method and metric, a particle state can be determined, predicted and controlled prior to a PT, as implemented in the method article. This is by determining the entanglement length and its divergence between two lensing events relative to their lens distance as observed and analyzed at the PT level. This is done through CNOT lens coding and entanglement entropy (EE) measure based on density matrices and steps to encode and decode states. The keys for this measurement are lenses, photopropes, photodetectors and a CNOT gate built by contacting CNTs to a superconductor. This is where the number of particle spins is recorded by counter particles once the photopropes and particles interact. For a high-temperature focused system approaching a CPT, all particles assume a high-energy state (a great momentum). The prediction of slow particles with low-energy states by the DFC algorithm is possible when entangled with high-energy particles by polarized photons through the gate over a lens distance. For a low-temperature focused system approaching a QPT, the converse applies. As the system evolves in its distribution of states, those particles not reaching a desirable state, i.e., the probability of observing a spin up or spin down (GS or ES) outcome at the decoding step, can be rerouted by the heat engine to satisfy a desirable outcome. This establishes a GS or ES energy profile to access and classify states by a classifier. After learning the profile, the classifier decodes and predicts the system state, as presented by a quantum field lens coding algorithm (QF-LCA) in the method article [3].

The simulated heat engine by DFC as a QF-LCA and its classifier(s) predicts and reroutes particle energy paths on any logarithmic input-output scale. This method can improve DFC algorithms to determine which particles participate in a PT, as the next system state evolves and predicted. As a result, computations via such algorithms maximize system efficiency through EE measure on micro and macro levels of energy states distributed in an  $N$ -particle system.

## Acknowledgments

P. B. A. acknowledges Dr. W. Chen endorsement from the Institute of Theoretical Physics at ETH Zürich, on the Statistical Mechanics concepts. P. B. A. also acknowledges the University of Victoria Canada, for financial support. P. B. A. and T. A. G. thank Dr. T. Lu for his comments on the scalar field, dimensions and photonics, Eqs. (23)–(42), Dr. M. Laca for his comments on Eqs. (4)–(18), and the late Dr. F. Diacu for his input on phase transitions to parameterize their probabilities in the proposed computation model.

## Appendix A Visualized computation model

The observable events' summary from Figs. 1–5, is presented in Fig. A.2. From the top left, thermodynamic events are simulated according to Secs. 1–7 and expected to deliver their data to a realtime observer during a QDF experiment. The simulation of the QDF circuit thermodynamics starts from the lower-left of the figure with probability measure after data submission and analysis. The goal and objectives, Sec. 2, are achieved on the right side where DFC software and hardware outputs meet with the analyzed data to train the QF-LCA algorithm. The details are discussed in our method article [3], including the quantum AI approach upon data analysis to validate the findings of this paper, the QDF model and application from [1]. In Fig. A.2 conclusion, the QDF application and its usefulness after computational thermodynamics of the QDF system are finalized by doubling the probability outcome of the thermodynamic events. This enables a decision to make upon observation of energy paths, reroute or create them to obtain greater system efficiencies and performance, see Appdx. B.

### A.1 Data availability

All data needed to reproduce the results are available from the main text equations, as validated via online simulation engines and toolkits [101]. For DFC algorithms 1 and 2, the supplementary information as code and simulation is available at [2, 3]. Additional data request may be forwarded to P. B. Alipour (phibal12@uvic.ca), such as simulation results, analysis and validation of the coding method.

### A.2 Code availability

All information needed to write code that can reproduce the results are available in [2, 3], and the main text and supplementary information by [2].

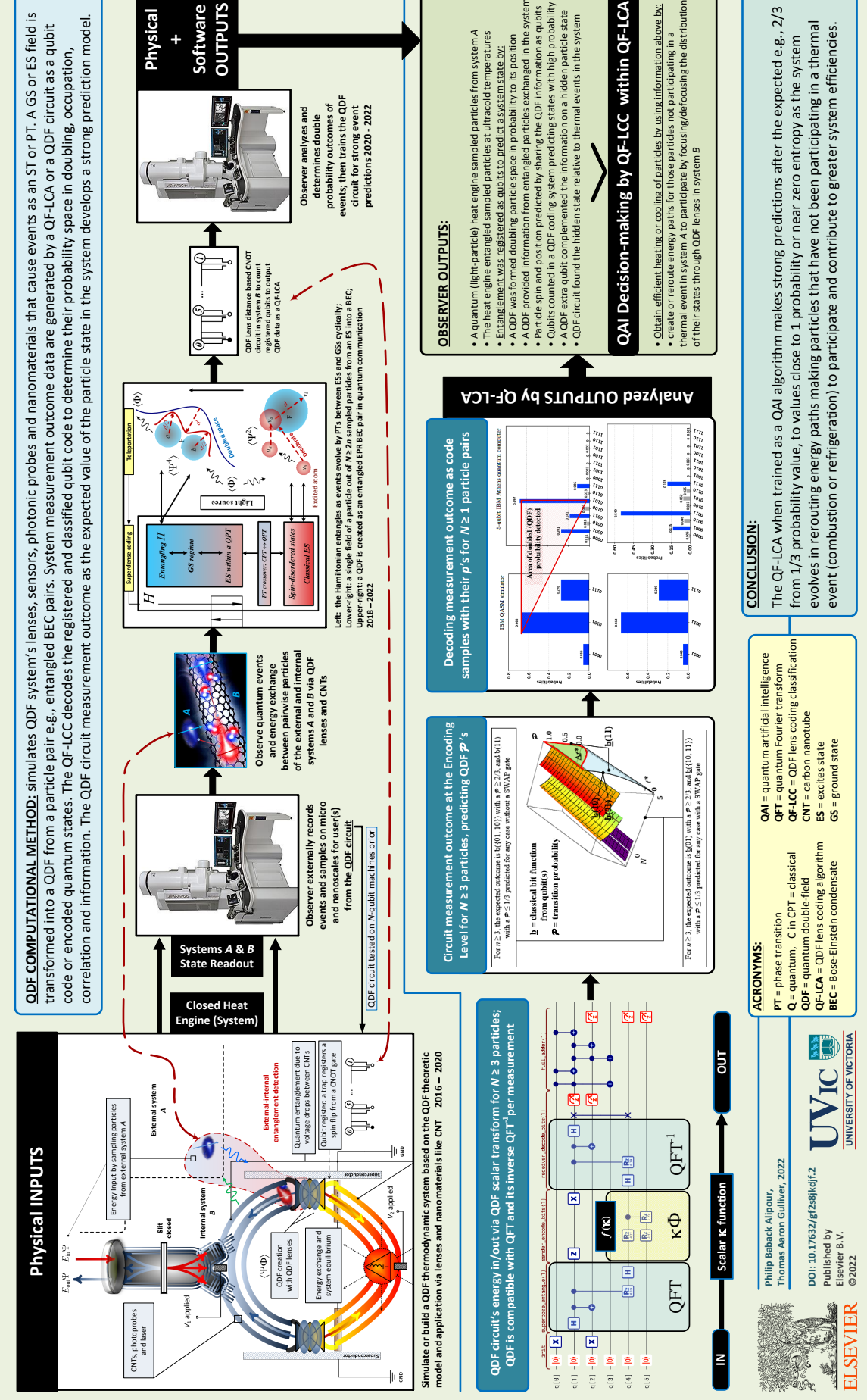


**Fig. A.** Visualized abstract of the QF-LCA given the simulated thermodynamic events in the system. The simulation begins in the upper figure from left to right as summarized from Secs. 1–7. The computational method is focused on the lower part of the figure, from the left is the QDF circuit, middle is the measurement outcome relative to probability measures for the simulated events from the circuit, as in Sec. 8. Both upper and lower parts achieve the objectives as listed under the (expected) observer outputs.

## Appendix B Popular summary

System efficiency and performance are paramount in engines manufactured for, e.g., refrigerators, cars, jets, and in communications, computers, the internet, etc. The more speed and energy-efficient the system with low power consumption, the more positive impact in reducing carbon footprint as an environmental-friendly solution.

We propose a field computation model to simulate a heat engine equipped with a quantum circuit to address systems with less efficiency, such as particles that do not participate in a combustion, refrigeration or any other thermodynamic event for a desired energy output. The engine is simulated to get the engine's nano-materials and lenses the energy readouts and analyze the data for those particles that are not fully participating in the thermodynamic event, as an uncertainty measure or entropy. The input energy levels are encoded and classified through information transfer by entangled particle fields, such as light probing, pairwise particle counting and interaction, which provide information to a user or a system agent as an alternative energy path. The agent then decides which particles to participate in the energy path or areas of the system for maximum efficiency.

In this simulation, the lens transforms particle fields to one another, while information is transmitted by doubling the event's probability to  $P \geq 2/3$  for each light-particle double-field transformation, based on its model from [1]. This probability measure projects a reliable prediction for a desired energy output.

The implications of this work are advances in communications and computational thermodynamics on a macroscale, e.g., observe and simulate planetary climate change, planets, stars, and on a micro-scale, e.g., simulate thermal or quantum mechanical micro-black holes (via BEC), and on a nanoscale, e.g., observe and simulate the cooling of atoms down to BEC and entangled BEC pair creation to reliably predict their next energy state.

## References

- [1] P. B. Alipour, T. A. Gulliver, Quantum Double-field Model and Application, Elsevier BV, 4233203 (2022) 28. DOI:10.2139/ssrn.4233203.
- [2] P. B. Alipour, T. A. Gulliver, Dataset for Quantum Double-field Model and Application, Mendeley Data, Elsevier BV (2022) V1, DOI:10.17632/gf2s8jkdfj.1
- [3] P. B. Alipour, T. A. Gulliver, A Quantum Field Lens Coding and Classification Algorithm to Predict Measurement Outcomes, *Invited only publication in MethodsX*, Elsevier BV (2022), MEX-D-22-00201.
- [4] Z.-K. Liu, Computational thermodynamics and its applications, *Acta Mat.*, Elsevier BV, 200 (2020) 745–792.
- [5] P. Strasberg, G. Schaller, T. Brandes, M. Esposito, Quantum and Information Thermodynamics: A Unifying Framework Based on Repeated Interactions, *Phys. Rev. X*, 7 (2017) 021003.
- [6] G. J. Schmitz, U. Prahl (Eds.), *Integrative Computational Materials Engineering, Concepts and Applications of a Modular Simulation Platform* (Wiley-VCH, 2012), Chaps. 1, 3, 9.
- [7] J. D. Whitfield, J. Yang, W. Wang, J. T. Heath, B. Harrison, Quantum Computing 2022, *Quant. Phys.* arXiv:1712.07326 (2022).
- [8] Z. Gao, *Computational Modeling*, Retrieved from Nat. Inst. of Biomed. Imag. and Bioeng. (NIBIB) in 2021 at: <https://www.nibib.nih.gov/science-education/science-topics/computational-modeling#pid-1191> [Accessed, 2022].
- [9] S. Rastgoo, M. Requardt, Emergent space-time via a geometric renormalization method, *Phys. Rev. D* 94 (12) (2016) 124019.
- [10] M. Damian, S. Pandit, S. Pemmaraju, *Lecture Notes in Computer Science* (Springer, 2006) 4305, Secs. 4–5.
- [11] Y-L. Xu, X-M. Kong, Z-Q. Liu, C-Y. Wang, Quantum entanglement and quantum phase transition for the Ising model on a two-dimensional square lattice, *Physica A* 446 (2016) 217–223.
- [12] P. Pessoa, C. Cafaro, Information geometry for Fermi–Dirac and Bose–Einstein quantum statistics, *Physica A* 576 (2021) 126061.
- [13] P. Frąckiewicz, A. G. M. Schmidt, *N*-person quantum Russian roulette, *Physica A* 401 (2014) 8–14.
- [14] J. S. Briggs, A derivation of the time-energy uncertainty relation, *IOP J. of Phys., Conf. Series* 99 (2008) 012002.
- [15] M. G. Vasin, V. M. Vinokur, Bose system critical dynamics near quantum phase transition, *Physica A* 575 (2021) 126035.
- [16] Committee on AMO 2010, *Controlling the Quantum World: The Science of Atoms, Molecules, and Photons*, Chaps. 3, 5–7.
- [17] E. Grumblung, M. Horowitz (Eds.), *Quantum Computing: Progress and Prospects* (National Academies Press, USA, 2019), Chaps. 2, 3, 5.
- [18] P. Ball, (Oxford Univ. Press, 2018), Jian-Wei Pan: building the quantum internet, *Nat. Sci. Rev.* 6 (2019) 2.
- [19] S. M. Girvin, K. Yang, *Modern Condensed Matter Physics* (Cambridge Univ. Press, 2019), Chaps. 3, 7, 8, 17, and Appx. F.
- [20] F. C-Bonneau, Tsallis entropy for assessing quantum correlation with Bell-type inequalities in EPR, *Physica A*, 414 (2014) 204–215.
- [21] P. Pessoa, C. Cafaro, Information geometry for Fermi–Dirac and Bose–Einstein quantum statistics, *Physica A*, 576 (2021) 126061.
- [22] J. H. Kim, T. V. Pham, J. H. Hwang *et al.*, Boron nitride nanotubes: synthesis and applications. *Nano Convergence* 5 (2018) 17.
- [23] H. L. Stern, Q. Gu, J. Jarman *et al.*, Room temperature optically detected magnetic resonance of single defects in hexagonal boron nitride, *Nat. Commun.* 13 (2022) 618.
- [24] B. Dumé (Editor), *Bose-Einstein condensate forms in nanoparticle lattice*, *Phys. World*, IOP J. (2018).
- [25] Z. Nussinov, Macroscopic length correlations in non-equilibrium systems and their possible realizations, *Nuc. Phys. B* 953 (2020) 114948.
- [26] E. Grumblung, M. Horowitz (Eds.), *Quantum Computing: Progress and Prospects* (National Academies Press, USA, 2019), Chaps. 2, 3, 5.
- [27] C-R. Wie, Two-qubit Bloch Sphere, *Phys. 2* (2020) 3, pp. 383–396.
- [28] R. B. Griffiths, *Phys. Rev. A* 96 (2017) 032110; *Quantum Measurements and Contextuality*, Carnegie-Mellon Univ., USA (2018).
- [29] S. Ghosh, T. C. H. Liew, Quantum computing with exciton-polariton condensates, *NPJ Quant. Info.* 6 (2020) 16.
- [30] H. T. Ng, C. K. Law, P. T. Leungm, Quantum-correlated double-well tunneling of two-component Bose-Einstein condensates, *Phys. Rev. A* 68 (2003) 013604.
- [31] D. Sych, A complete basis of generalized Bell states, *N. J. Phys.*, IOP Sci. 11 (2009) 013006.
- [32] J. L. E. da Silva, G. B. da Silva, R. V. Ramos, The Lambert-Kaniadakis  $W_k$  function, *Phys. Lett. A* 384 (2020) 126175.
- [33] J. D. Norton, *Evolution in time of a wave, Einstein for Everyone* (Nullarbor Press, Pittsburgh Univ., USA, 2020), Chap. 42.
- [34] R. Blume-Kohout, S. Croke, M. Zwolak, Quantum data gathering, Quantum data gathering *Sci. Rep.* 3 (2013) 1800.
- [35] A. Borzi, G. Ciaramella, M. Sprengel, *Formulation and Numerical Solution of Quantum Control Problems* (SIAM, 2017), Chaps. 2.6–2.8.
- [36] W-M. Liu and Emmanuel Kengne, *Schrödinger Equations in Nonlinear Systems* (Springer, 2019), Chaps. 1.3, 10.5 and 10.6.3.
- [37] L. D. Carr, *Understanding Quantum Phase Transitions* (CRC Press, USA, 2010), Secs. 1.2, 1.6, 2–2.4.
- [38] T. Kopp, F. J. Seco, S. Schiller, P. Wölflle, Superconductivity in the single-band Hubbard model: mean-field treatment of slave-boson pairing, *Phys. Rev. B*, 38 (1988) 11835.
- [39] W-W. Yang, Y. Zhong, H-G. Luo, Benchmarking the simplest slave-particle theory with Hubbard dimer, *Chin. Phys. B*, IOP Sci. 28 (2019) 107103.
- [40] J. Stolze, D. Suter, *Quantum Computing* (Wiley-VCH, 2004), 1st ed., pp. 1–62, 217, Chaps. 6–8, 10–13.

- [41] F. Mandl, G. Shaw, *Quantum Field Theory* (Wiley Press, 2010), 2nd ed., pp. 2–24, 40–97, 110–126.
- [42] C. Lacroix, P. Mendels, F. Mila, *Introduction to Frustrated Magnetism, Materials, Experiments, Theory* (Springer, 2016), Chaps. 1–3, 23.
- [43] J. O. Haerter, K. Sneppen, *Statistical Mechanics, the Ising Model and Critical Phenomena, Complex Physics*, (Niels Bohr Institute, Denmark, 2017), Chap. 1.
- [44] R. Iomicioiu, Schrödinger's Cat: Where Does The Entanglement Come From?, *Quanta* **6** (2017) 57.
- [45] D. Angelakis, M. Christandl, A. Ekert, Quantum Information Processing: From Theory to Experiment, *IOS Press* **199** (2006) 109–112.
- [46] X. He *et al.*, Carbon nanotubes as emerging quantum-light sources, *Nat. Mat.* **17** (2018) 663–670.
- [47] T. K. Hakala *et al.*, Bose–Einstein condensation in a plasmonic lattice, *Nat. Phys.* **14** (2018) 739–744.
- [48] C. Bena, S. Vishveshwara, L. Balents, M. P. A. Fisher, Quantum Entanglement in Carbon Nanotubes, *Phys. Rev. Lett.* **89** (2002) 037901.
- [49] F. Ancilotto, M. M. Calbi, S. M. Gatica, M. W. Cole, BEC of He and H inside bundles of carbon nanotubes, *Phys. Rev. B* **70** (2004) 165422.
- [50] I. Khivrich, S. Ilani, Atomic-like charge qubit in a carbon nanotube, *Nat. Commun.* **11** (2020) 2299.
- [51] B. Hacker, S. Welte, S. Daiss, A. Shaukat, S. Ritter, L. Li, G. Rempe, Deterministic creation of entangled atom–light Schrödinger-cat states, *Nat. Photon.* **13** (2019) pp. 110–115.
- [52] Xi-Lin Wang, Y-H. Luo, H-L. Huang *et al.*, 18-Qubit Entanglement with Six Photons, *Phys. Rev. Lett.* **120** (2018) 260502.
- [53] A. Hellmanns, *IEEE Spectrum* (2018) as a summary for N. Friis *et al.*'s work, *Phys. Rev. X* **8** (2018) 021012.
- [54] R. Blümel, N. Grzesiak, N. Pisenti, K. Wright, Y. Nam, Power-optimal, stabilized entangling gate between trapped-ion qubits, *Quant. Info. NPI*, **7** (2021) 147.
- [55] C. H. Wong, E. A. Buntov, M. B. Guseva, R. E. Kasimova, V. N. Rychkov, A. F. Zatsepin, Superconductivity in ultra-thin carbon nanotubes, *Elsevier* **125** (2017) 509–515.
- [56] T-F. Zhang *et al.*, Broadband photodetector based on CNT thin film/single layer graphene Schottky junction, *Sci. Rep.* **6** (2016) 38569.
- [57] S. Suzuki, J. Inoue, B. Chakrabarti, *Quantum Ising Phases and Transitions in Transverse Ising Models* (Springer, 2013), Chaps. 2, 3, 7, 10.
- [58] G. Vidal, J. I. Latorre, E. Rico, A. Kitaev, Entanglement in Quantum Critical Phenomena, *Phys. Rev. Lett.* **90** (2003) 227902.
- [59] Y. Li, W. Pang, J. Xu, C. Lee, B. A. Malomed, L. Santos, Long-range transverse Ising model built with dipolar condensates in two-well arrays, *N. J. Phys.* **19** (2017) 013030.
- [60] D. D' Alessandro, *Introduction to Quantum Control and Dynamics* (Chapman & Hall, USA, 2008), pp. 62–67.
- [61] W. Li, L. Ding, R. Yu, T. Roscilde, S. Haas, Scaling behavior of entanglement in two- and 3D free-fermion systems, *Phys. Rev. B* **74** (2006) 073103.
- [62] B. Marcone, E. Orlandini, F. Toigo, F. Ancilotto, Condensation of helium in interstitial sites of carbon nanotubes bundles, *Phys. Rev. B* **74** (2006) 085415.
- [63] M. W. Cole, V. H. Crespi, G. Stan, C. Ebner, J. M. Hartman, S. Moroni, M. Boninsegni, Condensation of Helium in Nanotube Bundles, *Phys. Rev. Lett.* **84** (2000) 3883.
- [64] B. J. Dalton, J. Goold, B. M. Garraway, M. D. Reid, Quantum entanglement for systems of identical bosons, *IOP Phys. Scr.* **92** (2017) 023005.
- [65] Y. Jing *et al.*, Split spin-squeezed bose–einstein condensates, *N. J. Phys.* **21** (2019) 093038.
- [66] M. Chaudhary, M. Fadel, V. Ivannikov, T. Byrnes, Continuous variable teleportation protocol for split-squeezed Bose Einstein condensates, *AIP Conf. Proc.* **2241** (2020) 020010.
- [67] J. Dubail, J. L. Jacobsen, H. Saleur, Conformal field theory at central charge, *Nuc. Phys. B* **3** (2010) 834.
- [68] C. H. Bennett, G. Brassard, C. Crepeau, R. Josza, A. Peres, W. K. Wootters, Teleporting an unknown quantum state via dual classical and Einstein-Podolsky-Rosen channels, *Phys. Rev. Lett.* **70** (1993) 1895.
- [69] C. M. Van Vliet, *Equilibrium and Nonequilibrium Statistical Thermodynamics* (WSP, 2010), pp. 5–42, 102, 540, 707.
- [70] P. A. Belov, A. A. Nazarov, A. O. Sorokin, Numerical determination of the CFT central charge in the site-diluted Ising model, *J. Phys. Conf. Ser.* **929** (2017) 012037.
- [71] I. V. Bondarev, A. V. Meliksetyan, Possibility for exciton Bose-Einstein condensation in carbon nanotubes, *Phys. Rev. B* **89** (2014) 045414.
- [72] Y. Zhuang, J. Wen, N. Tanga, M. Li, L. Lv, Y. Du, High-temperature ferromagnetism of helical carbon nanotube, *AIP Adv.* **3** (2013) 052112.
- [73] A. Das, P. Bhattacharya, J. Heo, A. Banerjee, W. Guo PNAS, **110** *8* (2013) 2735–2740.
- [74] R. Howl, R. Penrose, I. Fuentes, Exploring the unification of quantum theory and general relativity with a BEC, *N. J. Phys.* **21** (2019) 043047.
- [75] G. A-Camelia, S. Majid, Waves on Noncommutative Spacetime and Gamma-Ray Bursts, *J. Mod. Phys. A* **15** (2000) 27.
- [76] E. Castellanos, T. Matos, Klein-gordon fields and bose-einstein condensates, *Int. J. Mod. Phys. B* **27** (2013) 1350060.
- [77] A. Hamma, W. Zhang, S. Haas, D. A. Lidar, Entanglement, fidelity, and topological entropy in a quantum phase transition to topological order, *Phys. Rev. B* **77** (2008) 155111. Also, <https://pitp.phas.ubc.ca/confs/qc08/talks/haas.pdf>.
- [78] T. Kuwahara, I. Arad, L. Amico, V. Vedral, Local reversibility and entanglement structure of many-body ground states, *Quan. Sci. Tech.* **2** (2017) 015005.
- [79] M. A. Nielsen, and I. L. Chuang, *Quantum Computation and Quantum Information* (Cambridge Univ. Press, 2010), Chaps. 1, 2, 11, 12, pp. 97, 136–164, 309–424.
- [80] M. Enríquez, I. Wintrowicz, K. Z. Yczkowski, Maximally Entangled Multipartite States: A Brief Survey, *J. Phys. Conf. Ser.* **698** (2016) 012003.
- [81] J-L. Basdevant, J. Dalibard, *Quantum Mechanics* (Springer, 2006), 2nd ed., pp. 116–132, 309–342.
- [82] C. W. Myles (Condensed Matter Phys. Prof., Eng. Phys.), *Lecture Notes on Energy Conservation Theorems*, *Phys.* **5306**, Tech. Uni., USA (2004–2021).
- [83] D. McMahon, *Quantum Mechanics Demystified* (McGraw Hill, NY, USA, 2013), Chaps. 2, 8–11.
- [84] B. C. Hall, Grad. Texts in Math., *Quant. Theo. for Mathematicians* (Springer, USA, 2013), Chaps. 1–3, 11, 19.
- [85] G. Ekspong (Ed.), Nobel Lectures, Physics (1996–2000), *Nobel Lecture by W. D. Phillips, Dec. 8, 1997*, (WSP, SG, 2002), pp. 199–237.
- [86] B. Thaller, *Advanced Visual Quantum Mechanics* (Springer, 2005), Chaps. 2, 4–6.
- [87] W. P. Schleich, H. Walther, *Elements of Quantum Information*, (Wiley-VCH, 2007), Chap. 16.
- [88] J. Bird, C. Ross, *Mechanical Engineering Principles* (Routledge, UK, 4th ed., 2020), p. 42.
- [89] C. R. Nave, *Schrödinger Equation* and *Quantum oscillator*, redirected from Phys. World IOP J. (2009): <http://physicsworld.com/a/web-life-hyperphysics> [Accessed, 2018].
- [90] G. Acampora (EIC), Quantum machine intelligence, *Springer* **1** (2019) 1–3.
- [91] A. T. Sornborger, Quantum simulation of tunneling in small systems, *Sci. Rep.* **2** (2012) 597.
- [92] A. C-Lierta, José I. Latorre, D. Goyeneche, Quantum circuits for maximally entangled states, *Phys. Rev. A* **100** (2019) 022342.
- [93] J. Romero, J. P. Olson, A. A-Guzik, Quantum autoencoders for efficient compression of quantum data, *Quantum Sci. Technol.*, *IOP Sci.* **2** (2017) 045001.
- [94] H. Wang, Quantum algorithm for preparing the ground state of a system via resonance transition, *Sci. Rep.* **7** (2017) 16342.
- [95] M. Hanks, M. P. Estrella, W. J. Munro, K. Nemoto, Effective Compression of Quantum Braided Circuits by ZX-Calculus, *Phys. Rev. X* **10** (2020) 041030.
- [96] Y. Wang, Z. Hu, C. Sanders, S. Kais, Qudits and High-D Quantum Computing, *Front. Phys.* **8** (2020) 479.

- [97] G. R. Malik, R. P. Singh, B. K. Behera, P. K. Panigrahi, *First experimental demonstration of multi-particle quantum tunneling in IBM quantum computer*, *Quant. Phys.* arXiv:1712.07326 (2019); Main Ref. DOI: 10.13140/RG.2.2.27260.18569 (2019).
- [98] N. M. P. Neumann, *Classification using a two-qubit quantum chip*, *Quant. Phys.* arXiv:2004.10426 (2020).
- [99] R. Wezeman, N. Neumann, F. Phillipson, *Distance-based classifier on the Quantum Inspire*, Springer, Digitale Welt 4 (2020) 85–91.
- [100] G. B. Lesovik, I. A. Sadovskyy, M. V. Suslov, A. V. Lebedev, V. M. Vinokur, Arrow of time and its reversal on the IBM quantum computer, *Sci. Rep.* 9 (2019) 4396.
- [101] S. Wolfram, *Mathematica Simulation Systems* at: <https://www.wolframalpha.com> [Accessed, 2015–2020].
- [102] C. Dilmegani, *Quantum Artificial Intelligence*, <https://research.aimultiple.com/quantum-ai> [Accessed, 2021].
- [103] C. E. Shannon, *A Mathematical Theory of Communication*, Reprint from Bell Sys. Tech. J., 27 (1948).
- [104] V. N. Pokrovskii, A Derivation of the Main Relations of Nonequilibrium Thermodynamics, Hindawi Pub. Corp., UK, ISRN Thermodynamics, 2013 (2013) 906136.
- [105] J. A. Cortese, T. M. Braje, *Loading Classical Data into a Quantum Computer*, *Quant. Phys.* arXiv:1803.01958 and QIP J. 2018 (2018).
- [106] S. Deffner, S. Campbell, *Quantum Thermodynamics* (IoP, 2019), Chap 1.
- [107] J. Diazdelacruz, Quantum Relative Entropy of Tagging and Thermo-dynamic, *Entropy* 22 (2020) 138.
- [108] J. K-Flam, R. Sohal, L. Nie, Information scrambling with conservation laws, *Stat. Mech.* (2021) arXiv:1805.09607.
- [109] A. C-Lierta, J. S. Kottmann, Alán A-Guzik, Meta-Variational Quantum Eigensolver: Learning Energy Profiles of Parameterized Hamiltonians for Quantum Simulation, *Phys. Rev. X Quant.* 2 (2021) 020329.
- [110] S. Lu, M. C. Bañuls, J. I. Cirac, Algorithms for Quantum Simulation at Finite Energies, *Phys. Rev. X Quant.* 2 (2021) 020321.
- [111] D. Koch, B. Martin, S. Patel, L. Wessing, P. M. Alsing, Demonstrating NISQ era challenges in algorithm design on IBM's 20-qubit quantum computer, *AIP Adv.* 10 (2020) 095101.
- [112] T. D. Bradley (Ph.D. Candidate in Math. and Quaunt. Theo.). *What is applied category theory?* (2019) pp. 9–11, 22, 43–50, NY Univ., USA; pp. 5–6 of *Tensor Product on Quanatum Particles* (2020).